

# Vision restoration in photoreceptor-degenerated mice and macaque monkeys using nanowires

**Ruyi Yang**

Fudan University

**Peng Zhao**

Fudan University

**Liyang Wang**

Fudan University

**Chenli Feng**

Fudan University

**Chen Peng**

Fudan University

**Zhexuan Wang**

Fudan University

**Yingying Zhang**

East China Normal University

**Minqian Shen**

Fudan University

**Kaiwen Shi**

Fudan University

**Shi-Jun Weng**

Fudan University

**Chunqiong Dong**

Fudan University

**Yuqing Chen**

Fudan University

**Fu Zeng**

Fudan University

**Tianyun Zhang**

Fudan University

**Luoyin Fu**

Fudan University

**Ruoxi Ma**

Fudan University

**Fei Wang**

Huashan Hospital

**Su Jiang**

Fudan University

**Wendong Xu**

Fudan University

**Gang Wang**

Beijing Institute of Basic Medical Sciences

**Gengfeng Zheng**

Fudan University <https://orcid.org/0000-0002-1803-6955>

**Aihua Chen**

East China Normal University

**Fei Yuan**

Fudan University

**Yuanzhi Yuan**

Fudan University

**Biao Yan**

Fudan University <https://orcid.org/0000-0003-3252-2965>

**Jiayi Zhang (✉ [jiayizhang@fudan.edu.cn](mailto:jiayizhang@fudan.edu.cn))**

Fudan University <https://orcid.org/0000-0002-1575-0723>

---

**Article**

**Keywords:**

**Posted Date:** March 1st, 2022

**DOI:** <https://doi.org/10.21203/rs.3.rs-492941/v2>

**License:** © ⓘ This work is licensed under a Creative Commons Attribution 4.0 International License.

[Read Full License](#)

---

1 [Submitted as an *Article* to the editor of *Nature Biomedical Engineering*]

2 **Vision restoration in photoreceptor-degenerated mice and macaque monkeys using**  
3 **nanowires**

4  
5 *Ruyi Yang<sup>1</sup>, Peng Zhao<sup>1</sup>, Liyang Wang<sup>1</sup>, Chenli Feng<sup>1</sup>, Chen Peng<sup>2</sup>, Zhexuan Wang<sup>1</sup>, Yingying*  
6 *Zhang<sup>3</sup>, Minqian Shen<sup>1</sup>, Kaiwen Shi<sup>1</sup>, Shijun Weng<sup>1</sup>, Chunqiong Dong<sup>1</sup>, Yuqing Chen<sup>1</sup>, Fu Zeng<sup>3</sup>,*  
7 *Tianyun Zhang<sup>1</sup>, Luoyin Fu<sup>1</sup>, Ruoxi Ma<sup>1</sup>, Fei Wang<sup>4</sup>, Su Jiang<sup>4</sup>, Wendong Xu<sup>4</sup>, Gang Wang<sup>5</sup>,*  
8 *Gengfeng Zheng<sup>2</sup>, Aihua Chen<sup>3</sup>, Fei Yuan<sup>1</sup>, Yuanzhi Yuan<sup>1,\*</sup>, Biao Yan<sup>1,\*</sup>, Jiayi Zhang<sup>1,\*</sup>*

9  
10 *<sup>1</sup>State Key Laboratory of Medical Neurobiology, MOE Frontiers Center for Brain Science, Institutes*  
11 *of Brain Science, Department of Ophthalmology, Zhongshan Hospital, Shanghai Medical College,*  
12 *Fudan University, Shanghai 200032, China.*

13 *<sup>2</sup>Laboratory of Advanced Materials, Department of Chemistry, Faculty of Chemistry and Materials*  
14 *Science, Fudan University, Shanghai 200240, China.*

15 *<sup>3</sup>Key Laboratory of Brain Functional Genomics (Ministry of Education), East China Normal*  
16 *University, Shanghai 200062, China*

17 *<sup>4</sup>Department of Hand Surgery, National Clinical Research Center for Aging and Medicine, Huashan*  
18 *Hospital, Institute of engineering and application technology, Fudan University, Department of*  
19 *Hand and Upper Extremity Surgery, Jing'an District Center Hospital, Shanghai Clinical Medical*  
20 *Center for Limb Function Reconstruction, Shanghai 200040, China.*

21 *<sup>5</sup>Center of Brain Sciences, Beijing Institute of Basic Medical Sciences, Beijing 100850, China*

22  
23 *The first four authors contributed equally to this work.*

24  
25 *\*Corresponding authors: Jiayi Zhang, Biao Yan and Yuanzhi Yuan; E-mail addresses:*  
26 *[jiayizhang@fudan.edu.cn](mailto:jiayizhang@fudan.edu.cn), [biaoayan@fudan.edu.cn](mailto:biaoayan@fudan.edu.cn), and [yuan.yuanzhi@zs-hospital.sh.cn](mailto:yuan.yuanzhi@zs-hospital.sh.cn).*

27  
28 **Abstract**

29 Photoreceptor degeneration diseases, such as retinitis pigmentosa and age-related macular  
30 degeneration, are major causes of blindness. Photovoltaic devices or materials activates retinal cells  
31 in response to light, hence are promising retinal prosthesis in treating blind patients. The restoration  
32 of image-forming vision with high sensitivity is the key. Here we demonstrated that Au nanoparticle-

33 coated titania ( $\text{TiO}_{2-x}$ ) nanowire (NW) arrays can restore vision in blind mice and non-human  
34 primates with photoreceptor degeneration. We first showed that blind mice with subretinal implant  
35 of NW arrays were capable of detecting static, moving and flashing objects with low light intensity  
36 threshold for 22 months, having a visual acuity of 0.3 cpd (0.4 cpd in normal mice). Results in  
37 chronic *in vivo* calcium imaging in primary visual cortex (V1) collectively suggested the plastic  
38 change in V1 neurons as well as the improvement in visual information encoding for natural images  
39 after NW implant. What's more, macaque monkeys with subretinal implant of NW arrays were  
40 capable of detecting an LED of  $0.5^\circ$  in diameter at  $10 \mu\text{W}\cdot\text{mm}^{-2}$  in visually-guided saccade  
41 experiments. Our findings opened up the possibility to utilize nanomaterials as artificial  
42 photoreceptors to ameliorate visual deficits of patients with photoreceptor degeneration.

### 43 **Introduction**

44 Photoreceptor degeneration caused by retinitis pigmentosa (RP) or age-related macular  
45 degeneration (AMD) has long been a major cause of blindness. Despite the loss of photoreceptors  
46 in the retina, the remaining retinal cells as well as their projections to the brain are preserved from  
47 the disease. In the past decade, success in treating Leber congenital amaurosis (LCA) using AAV-  
48 based treatment has opened up opportunities in gene therapy <sup>1,2</sup>. Recent studies using genetic and  
49 stem-cell based strategies have made great progress in providing proof-of-principle evidences to  
50 restore light sensitivity in photoreceptor-degenerated mice <sup>3-7</sup>. One clinical study demonstrated that  
51 with the help of engineered goggles, an RP patient exhibited partial restoration of vision with retinal  
52 expression of optogenetic proteins <sup>8</sup>. Challenges are in the restoration of image-forming vision with  
53 high sensitivity, as well as biosafety issues <sup>9</sup>.

54 The multielectrode stimulation devices turn light signals in the external world into patterned  
55 electrical currents and stimulate the remaining retinal cells to establish visual perception in blind  
56 patients with late-stage photoreceptor-degenerating diseases <sup>10</sup>. Argus II, a device with 60 pixels,  
57 received market approval in both Europe and the United States. The epiretinal implant of Argus II  
58 enabled blind patients to not only perceive light but also perform certain visual tasks <sup>11-13</sup>, despite  
59 issues of limited visual acuity and safety profile in multicenter studies <sup>14</sup>. Similar issues occurred to  
60 subretinal implant Alpha AMS <sup>15,16</sup>. These early efforts in retinal prosthesis were followed by

61 subretinal implant IRIS II with 378-pixel electrical stimulation (each pixel is 100  $\mu\text{m}$  in diameter)  
62 in the retina<sup>17,18</sup>. With the assistance of video glasses that turns visible light into pulsed near-infrared  
63 light, patients achieved better visual acuity than those implanted with Argus II<sup>19</sup>. Neuroprosthesis  
64 with multichannel electrical stimulation device implanted intracranially into V1 also enabled form  
65 vision in both monkey and human<sup>20,21</sup>, despite a more invasive surgical procedure comparing to  
66 retinal prosthesis. Novel materials including organic photovoltaic and injectable nanoparticles  
67 provided proof-of-principle evidence for light perception in blind mice and shed light onto the next  
68 generation retinal prosthesis with improved surgical procedure and spatial resolution<sup>22-25</sup>. However,  
69 unlike semiconductor devices with tunable stimulation current, photoactive materials often exhibit  
70 limited light sensitivity.

71 We previously developed Au nanoparticle-decorated titania nanowire arrays (Au-TiO<sub>2</sub> NW  
72 array), in which each NW was roughly 100 nm in diameter and 2  $\mu\text{m}$  in length, with a similar  
73 physical size to photoreceptors. NW array converts UV, blue and green light into photocurrent to  
74 activate retinal ganglion cells in retinal degenerated 1 knockout (*rd1*<sup>-/-</sup>)/cone diphtheria toxin  
75 subunit-A (*cDTA*) blind mice, with light intensity threshold as low as 10  $\mu\text{W}\cdot\text{mm}^{-2}$  and a spatial  
76 resolution of 100  $\mu\text{m}$  *in vitro*<sup>26</sup>. The performance of the NW array in restoring image-forming vision  
77 *in vivo*, and more importantly, the potential for clinical application, is yet to be evaluated.

78 In this study, we developed Au@TiO<sub>2-x</sub> NW arrays (referred to as NW array below) with an  
79 enhanced UV-visible absorbance profile compared to Au-TiO<sub>2</sub> NW array. We showed NW-  
80 implanted blind mice had a visual acuity of 0.3 cpd and recognized static, moving and flashing  
81 objects in the two-choice box, respectively. One important question rarely addressed is the coding  
82 of visual information in animals with retinal prosthesis. Interestingly, we found that the number of  
83 light-responsive V1 neurons peaked at 1 week post implant surgery, and these light-responsive V1  
84 neurons responded to natural images in a similar way to those in normal mice. These evidence  
85 collectively indicate that image-forming vision was restored. Finally, we implanted NW arrays into  
86 the subretinal space of macaque monkey and showed that NW arrays have good biocompatibility.  
87 Visually-guided saccade to the NW-implanted area suggested the perception of an LED of 0.5° in  
88 diameter at a light intensity as low as 10  $\mu\text{W}\cdot\text{mm}^{-2}$ . Our study provided evidence for a novel retinal  
89 prosthesis material with high sensitivity.

90

## 91 **Results**

### 92 **Improved photocurrent of Au@TiO<sub>2-x</sub> NW arrays**

93 The TiO<sub>2-x</sub> NW arrays were prepared by hydrothermal growth and subsequent thermal  
94 annealing in H<sub>2</sub>/Ar to create oxygen vacancies. Au nanoparticles were then in situ reduced and  
95 deposited on the NW surface to obtain Au@TiO<sub>2-x</sub> NW arrays. The X-ray diffraction (XRD,  
96 Extended Data Fig.1a) pattern presented two peaks at 36.3 degrees and 63.1 degrees that matched  
97 well with rutile TiO<sub>2</sub> (101) and (002) planes. The NW arrays were composed of highly-dense single  
98 NW arrays with average lengths of ~ 2.5 μm and diameters of ~ 100 nm (Extended Data Fig.1b, c).  
99 High-resolution transmission electron microscopy (HRTEM) images showed the lattice spacing of  
100 the dark nanoparticles and NW arrays were 0.235 and 0.246 nm (Extended Data Fig.1c and inset),  
101 corresponding to cubic-phase Au (111) planes (JCPDS# 00-001-1172) and rutile-phase TiO<sub>2</sub> (101)  
102 planes (JCPDS# 01-088-1175), respectively. The spherical aberration-corrected HAADF-STEM  
103 image (Extended Data Fig.1d) showed the array of bright Ti (highlighted by blue spheres) and dark  
104 O (highlighted by red spheres) contrast on rutile TiO<sub>2</sub> (101) planes. The extracted intensity from the  
105 yellow dashed line of the fourth O atom greatly decreased (Extended Data Fig.1e), indicating the  
106 oxygen vacancies<sup>27</sup>. The existence of oxygen vacancies was further confirmed by X-ray  
107 photoelectron spectroscopy (XPS, Extended Data Fig.1f), in which the modified Au@TiO<sub>2-x</sub>  
108 presented an additional shoulder peak centered at ~ 532.5 eV<sup>28</sup>.

109 When illuminated by UV (375/28 nm, 292.99 μW·mm<sup>-2</sup>), blue (470/20 nm, 318.47 μW·mm<sup>-2</sup>),  
110 green (546/12 nm, 420.38 μW·mm<sup>-2</sup>) or red (697/30 nm, 331.21 μW·mm<sup>-2</sup>) light, the average  
111 photocurrents of the newly fabricated NW arrays were about 13000, 1300, 1100 and 30 pA,  
112 respectively (Extended Data Fig.2a-b), which is consistent with its adsorption spectrum (Extended  
113 Data Fig.2c). The photocurrents under UV, blue and green light increased by 5 ~ 7 times compared  
114 to those reported in our previous study<sup>26</sup> (Extended Data Fig.2d).

115 To confirm that NW arrays elicit light-evoked responses to function as artificial photoreceptors,  
116 we utilized *rd1<sup>-/-</sup>/cDTA* mice (referred to as blind mice below) whose rod and cone photoreceptors  
117 were completely gone by P50<sup>26</sup> (referred to as blind mice, Extended Data Fig.2e). Retinal ganglion  
118 cells (RGCs) of blind mice retina did not respond to UV, blue or green light. When NW arrays were  
119 attached to the blind retina, the RGCs of blind mice were activated by UV, blue or green light,

120 respectively (Extended Data Fig.2f-h).

121

## 122 **Localization of light source in NW-implanted blind mice**

123 Inspired by multiple visual tests used in human clinical trials with retinal prostheses implant<sup>15,</sup>  
124 <sup>30, 31</sup>, in which patients were asked to recognize various objects in blank background, we designed  
125 choice-box-based experiments to assess visual functions in mice. In our choice-box experiments,  
126 visual stimuli were delivered as it would naturally occur under natural circumstances.

127 In a rectangular box, two visual stimuli were projected onto one side of the box, and the  
128 opposite side was installed with one water port (Fig.1a). The behavior experiments were consisted  
129 of training and testing trials (Fig.1b). During the training trials, 2 ~ 3 seconds of random after tone  
130 1 (a preparation cue), visual stimuli were turned on for 20 sec (defined as reaction time). If the mice  
131 touched the target area corresponding to the pre-selected visual stimulus (defined in each of the  
132 following experiments) within 20 sec, the trial was defined as “correct”. Tone 2 (a cue for water  
133 reward) was provided and the mice received a water reward . If mice did not touch the screen (miss)  
134 or touch areas outside the target area (wrong), they would not get a water reward. When the miss  
135 rate (percentage of “miss” trials across all trials) becomes less than 50% for more than 3 days, the  
136 behavior paradigm was switched to testing trials, in which reaction time was 10 sec (Fig.1b). Correct  
137 rate was calculated in testing trials.

138 We implanted NW arrays subretinally into blind mice as previously shown for behavioral  
139 tests<sup>26</sup>. Light localization test was conducted in human subjects implanted with Argus II or AMS  
140 alpha. 96% of patients with Argus II implant and 78% patients with AMS alpha implant performed  
141 statistically better with the device switched on <sup>12,31</sup>. In the choice-box, LEDs with near UV, green  
142 or blue light emissions were used as visual stimuli, respectively (Fig.1c). In each trial, one of the  
143 two LEDs were turned on. If mice touched the target area (6 cm in diameter centered at the on-LED)  
144 corresponding to the ON LED, they would receive a water reward (correct) (Extended Data Movie  
145 1). All mice used in the light localization test were over 3 months old.

146 The correct rate (correct trials divided by all trials) of normal mice was 94.17%, 95%, 91.11%,  
147 for UV, green and blue light, respectively. The correct rate of blind mice implanted with glass was  
148 less than 25% for all three colors. For blind mice with NW arrays implant, the correct rate was  
149 82.71%, 82.29%, 83.85% for UV, green and blue light, respectively (Fig.1d). There was no

150 significant difference in the correct rate between NW-implanted mice and normal mice when light  
151 intensities were above  $3.31 \mu\text{W}\cdot\text{mm}^{-2}$  for blue light and  $6.75 \mu\text{W}\cdot\text{mm}^{-2}$  for green light (Fig.1e, f).  
152 Interestingly, blind mice with NW arrays implanted for 4 weeks tended to learn faster than those  
153 with NW arrays implanted for 1 weeks in the light source localization test (Extended Data Fig.3a-  
154 d). These data suggested that NW-implanted blind mice were capable of recognizing locations of  
155 light sources. Moreover, NW-implanted blind mice were capable of detecting static light that was  
156 on for up to 10 sec, confirming that image fading was less of a concern in our experiments.

157 Recent study reported melanopsin-expressing in ipRGC cells contribute to visual responses <sup>32</sup>.  
158 We found that the blind mice with glass implanted, in which ipRGCs were presumably functional,  
159 had a very low correct rate ( $< 25\%$ ), suggesting that melanopsin-expressing ipRGCs may not  
160 contribute to the localization of light under the light intensities we used in these experiments.

161

### 162 **Perception of moving objects in NW-implanted blind mice**

163 Clinical studies reported that 57% of patients with Argus II implant and 56% of patients with  
164 AMS alpha implant could detect the motion direction correctly, suggesting that detecting motion is  
165 more difficult than localizing light for patients with retinal prosthesis <sup>33,34</sup>. Moving light bars (9.60  
166 degrees in width, 6.85 degrees/sec) elicited transient spikes in the RGCs of blind mice retina  
167 attached to NW arrays *in vitro*, but not in the RGCs of blind mice (Fig.2a-f). Interestingly, light bars  
168 of 3.84 degree in width elicited the strongest responses in the RGCs of blind mice with NW arrays  
169 attached (Fig.2e, f).

170 We then examined the performance of NW-implanted blind mice in discriminating moving  
171 from static light bars in a choice-box-based behavioral test. After finishing light localization test in  
172 Fig. 1, mice were trained to touch the target area associated with a moving light bar to be rewarded  
173 (Fig.2g, Extended Movie 2). The correct rates of both normal and NW-implanted blind mice were  
174 84.79% in detecting moving light bars of 5.25 degree wide and 7.85 degrees/sec (Fig.2h-i, Extended  
175 Data Fig.3e), slightly lower than that in light localization test. Similar to normal mice, mice  
176 implanted with NW-array were good at detecting moving light bars of  $\sim 5$  degree wide (Fig.2i).

177 In Figure 2d, RGCs of blind mice with NW arrays attached responded to moving light bars  
178 with transient spiking activities, indicating that mice are capable of detecting moving objects with  
179 fast speed. Indeed, when presented with moving bars between 6.54 degrees/sec and 10.47

180 degrees/sec (5.25 degree in width), NW-implanted blind mice showed similar performance with  
181 normal mice (Fig.2j). Interestingly, NW-implanted blind mice failed to detect moving bars when the  
182 speed was below 6.54 degrees/sec (Fig.2j). These results suggested that NW-implanted blind mice  
183 can discriminate moving objects from static ones.

184

### 185 **Perception of flashing light in NW-implanted blind mice**

186 The patients with PRIMA implant reported persistent perception of flickering when stimulation  
187 frequencies were from 3 to 10 Hz, and flickering disappeared when the frequency was larger than  
188 60 Hz<sup>19</sup>. As reported in our previous study<sup>26</sup>, ~30% RGCs exhibited sustained firing in response to  
189 1-sec light stimulation and ~70% RGCs responded transiently to light stimuli, indicating that RGCs  
190 exhibited diverse temporal features in response to light<sup>26</sup>. In this study, we first examined the  
191 temporal resolution in RGCs of blind mice retina attached to NW arrays (Fig.3a). RGCs of both  
192 normal retina and NW arrays-attached blind retina responded to each flash faithfully at 1.25 Hz  
193 (Fig.3b-d). When stimulated by flashlight of 0.5 Hz ~ 5 Hz, at the firing rate and fraction of  
194 responses were similar between RGCs in normal and NW arrays-attached blind retina (Fig.3e, f).

195 To evaluate the temporal resolution of NW-implanted blind mice, mice were trained to touch  
196 the target area associated with flashing light (Fig.3g, Extended Data Fig.3f, Extended Movie 3). All  
197 mice were used in the light localization and moving object detection tests. Blind mice with NW-  
198 implant showed similar performance as normal mice at 2 to 3.3 Hz (Fig.3h-i). When the frequency  
199 of flash stimulation was either larger than 5 Hz or smaller than 1 Hz, the correct rate of NW-  
200 implanted blind mice was slightly smaller than that of normal mice, but still significantly higher  
201 than that of blind mice (Fig.3i).

202 After mice finished light localization, moving object and flashing light detection tests (22  
203 months after implant), we examined the histology of their retinæ by immunostaining the retinal  
204 cells at the implant site. The retinal ganglion cells (labeled by Brn3a), bipolar cells (labeled by PKC-  
205  $\alpha$ ) and amacrine cells (labeled by HPC) did not exhibit differences from those in normal (Fig.3j). In  
206 addition, microglia cells (labeled by Iba1) were not activated. These data suggested NW arrays  
207 exhibited favorable biocompatibility in mice.

208

### 209 **Visual acuity, contrast sensitivity and responses to natural scenes in NW-implanted blind mice**

210 Visual acuity and contrast sensitivity are the gold standards for clinical assessment of visual  
211 functions. Visual acuity is associated with the ability to resolve fine details and critical to pattern  
212 recognition, while contrast sensitivity is associated with the ability to distinguish subjects from  
213 background<sup>35</sup>. Previous clinical studies used Landolt C-rings to measure visual acuity in patients  
214 with retinal prostheses implant, and the best recorded visual acuity was 20/1260, 20/546 and 20/460  
215 by Argus II, AMS alpha and PRIMA, respectively<sup>19,33,34</sup>. To our knowledge, contrast sensitivity was  
216 not measured in any of the retinal prosthesis in clinical trials. In recent studies, the researchers used  
217 reprogramming techniques to recover youthful epigenetic information to restore the function of  
218 RGCs in the mice with glaucoma and the visual acuity increased from 0.20 to 0.27 cpd<sup>6</sup>.

219 To examine visual acuity and contrast sensitivity in NW arrays-implanted blind mice, we  
220 conducted an optomotor test (Fig.4a, Extended Movie 4). All mice used in visual acuity and contrast  
221 sensitivity test were over 11 months old. NW arrays were implanted into blind mice for more than  
222 9 months. In normal mice, the peak of contrast sensitivity was 0.1 cpd, and the average observed  
223 contrast sensitivity was 30 (or 3.3% contrast) (Fig.4b, c). The visual acuity of normal mice was  
224  $0.424 \pm 0.012$  cpd, which was consistent with previous reports<sup>36,37</sup>. We did not observe any  
225 optomotor response in blind mice. The average contrast sensitivity of NW-implanted blind mice  
226 was 5 (or 20% contrast) and the contrast sensitivity peak was at 0.05 cpd. The visual acuity of NW  
227 -implanted blind mice was  $0.313 \pm 0.015$  cpd (Fig.4b, c), with significant improvement from blind  
228 mice.

229 Previous studies found that sizes of receptive field are smaller where visual acuity is higher  
230 near the foveal region of the cortex in human<sup>38</sup>. To measure the size of the receptive field in V1  
231 neurons of NW-implanted blind mice, we conducted two-photon calcium imaging *in vivo* (Fig.4d).  
232 It was previously known that the dorsal nasal retina (where we implanted NW arrays) retinotopically  
233 project to medial V1<sup>39,40</sup>. We first confirmed the retinotopic projection from the retina to V1 by  
234 injecting Dil in the dorsal nasal retina and CTB 488 in medial V1. Indeed, Dil and CTB 488 signals  
235 overlapped in the dorsal lateral geniculate nucleus (Extended Data Fig.4). GCaMP6s were largely  
236 expressed in V1 neurons (Fig.4e). Receptive fields of neurons in V1 were mapped using a flashing  
237 blue square on a black background and calculated based on calcium signals after Gaussian fitting  
238 (Fig.4f-g). The average size of receptive fields in V1 neurons in normal mice was  $233 \pm 20$  deg<sup>2</sup>,  
239 which was similar to previous studies<sup>41,42</sup>. The average size of receptive fields in V1 neurons was

240  $403 \pm 86 \text{ deg}^2$  in blind mice with NW arrays implant (Fig.4h-i).

241 While drifting gratings used in the visual acuity experiment can be easily parameterized,  
242 natural scenes are ethologically more relevant. We measured the neuronal responses in V1 to natural  
243 scenes (Fig.4j-k). Fraction of natural-scene-responsive neurons was 72.36% and 16.69% in normal  
244 mice and blind mice, respectively. In NW arrays-implanted blind mice, fraction of natural-scene-  
245 responsive neurons (56.71%) was significantly larger than that in blind mice (Fig.4l). The patterns  
246 in population response exhibited a similar pattern between normal mice and NW-implanted blind  
247 mice (Fig.4k). Previous studies found that natural scenes can be efficiently represented by sparse  
248 coding in V1 neurons<sup>43,44</sup>. Responsive selectivity to different stimulus conditions is quantified by  
249 lifetime sparseness<sup>43,45,46</sup>. Neurons in NW-implanted blind mice had an average lifetime sparseness  
250 of 0.54, similar to that in normal mice (0.61) (Fig.4m). Together with results from the visual acuity  
251 and contrast sensitivity test, features of receptive fields and responses to natural scenes in V1  
252 neurons in NW-implanted blind mice collectively indicated that image-forming vision was largely  
253 restored in these mice.

254

### 255 **Long-term light-evoked responses in V1 neurons of NW-implanted blind mice**

256 Results from behavior experiments showed that mice implanted with NW were capable of  
257 conducting visual tasks for up to 9 months. Next, we aimed to investigate whether NW arrays  
258 elicited reliable light responses in V1 neurons over a long period of time. All mice used for two-  
259 photon recording were more than 4 months old. We conducted long-term two-photon recording via  
260 a glass cranial window (Extended Data Fig.5a) over V1 to continuously record activities from the  
261 same neuronal population 3, 5, 7, 14, 21, 28, 35, 42, 49, 56, 63, 70, 77 and 84 days after NW arrays  
262 implantation (Fig.5b, Extended Data Fig.5c, e, Extended Movie 5). The total number of recorded  
263 neurons did not show significant difference over time (Extended Data Fig.5b). 4 representative  
264 neurons were recorded throughout the entire recording period, among which 2 neurons started to  
265 respond to light one month after implantation and remained responsive 84 days after implantation  
266 (Fig.5c), while 2 other neurons stopped to respond to light one month after implant (Fig.5d). Before  
267 NW arrays implantation, V1 neurons in blind mice rarely respond to light (in comparison to normal  
268 mice, Fig.5e). 26.13% and 30.24% of these neurons exhibited light-evoked responses 5 and 7 days  
269 after implant surgery (Fig.5e). The changes in fluorescence ( $\Delta F/F_0$ ) of 28 representative light-

270 responsive neurons in two mice confirmed NW-array-mediated light responses (Extended Data  
271 Fig.5d, f). The fraction of light-responsive V1 neurons in NW arrays-implanted blind were  
272 significantly larger than that before implant surgery throughout 84 days of recording (Fig.5f). Note  
273 that the fraction of V1 neurons that responded to natural scenes (Fig. 4l) was much larger than that  
274 responded to flashing light, consistent with previous report <sup>46</sup>.

275 Interestingly, the fraction of light-responsive neurons peaked around 1 week after NW arrays  
276 implantation (Fig.5f). The average amplitude of calcium signals gradually increased over time while  
277 the latency of light responses decreased over time (Fig.5g, h), indicating that neurons in V1  
278 exhibited improvement in reliable coding of visual stimulus. These observations were consistent  
279 with previous studies, showing that the visual system can retain considerable plasticity beyond  
280 critical periods after blindness <sup>47</sup>.

281

#### 282 **NW exhibited good biocompatibility and stability in macaque monkey**

283 Long-term electrophysiological and behavioral experiments in NW-arrays implanted blind  
284 mice provided good prospects for translational study (Fig.1-5). Eyeballs of mice is much smaller  
285 than that of primates. More importantly, unlike primates, rodents have no fovea. We first conducted  
286 photocoagulation on the fovea and perifovea area in the right eye of a macaque monkey (named A)  
287 to induce focal photoreceptors degeneration (Fig.6a). Due to the COVID-19 pandemic, we were not  
288 able to conduct the implant surgery until 11 months after photocoagulation, when the presence of  
289 scar tissue in the photocoagulated area was not optimal for implant surgery. Instead of conducting  
290 surgery on the photocoagulated area, we identified an intact perifovea area to conduct implant  
291 surgery (indicated by the white arrow in Fig.6a).

292 Retinal prosthesis devices were implanted into a few mm sclerotomy following a 23-gauge  
293 vitrectomy <sup>17</sup>. One advantage of our study is that the NW-arrays implants can be cut into small  
294 pieces of customized sizes and remain functioning, due to the fact that light spots as small as 50  $\mu$ m  
295 elicited responses in RGCs <sup>26</sup>. To minimize the surgical trauma on the sclera and retina, NW arrays  
296 were cut into 0.40 mm  $\times$  1.80 mm pieces to be fit into the 23-gauge trocars for vitrectomy. We  
297 anesthetized Monkey A, performed vitrectomy, and detached the retina by subretinal injection of  
298 balanced salt solution (Lactated Ringer's solution), and made a retinotomy 3 mm in diameter. We  
299 delivered NW arrays through 23-gauge trocars using forceps and 8 pieces of NW arrays were

300 subretinally inserted. Finally, we injected perfluoro-decalin liquid over the NW arrays to stabilize  
301 the implant and injected silicone oil into the vitreous cavity to support retinal reattachment.  
302 Photocoagulations were conducted to seal the opening in the retina from retinotomy (indicated by  
303 green arrows in Fig.6a).

304 Color fundus photography taken 4 days, 3, 4, 6, and 8 weeks after implant surgery showed that  
305 NW arrays stayed in place (Fig.6a). Optical coherence tomography showed that the retina and NW  
306 arrays were in close contact throughout 8 weeks after implantation (Fig.6b). There were no  
307 significant changes in RPE cells in autofluorescence images (Fig.6c). Red-free fundus photography  
308 indicated no vascular abnormality in the retina and surrounding tissue after NW arrays implant  
309 (Fig.6d). These data suggested that NW arrays were stable in subretinal space and had good  
310 biocompatibility in the macaque monkey.

311

#### 312 **Visual stimulation elicited saccade behavior in macaque monkey with NW implant**

313 To examine whether NW arrays induced light-evoked responses in Monkey A, we conducted  
314 a monocular visually-guided saccade (VGS) behavioral test (Fig.7a). The non-surgical (left) eye  
315 was covered by eyeshade. Monkey A was trained to fixate at the central fixation point ( $0.5^\circ \times 0.5^\circ$ )  
316 at the beginning of the task (Extended Data Fig.6a). A target point ( $0.5^\circ \times 0.5^\circ$ ) appeared 1 sec later.  
317 When Monkey A shift its gaze from the central fixation into the target area (defined as a 15-degree  
318 circular region surrounding the target points, Extended Data Fig.6b) within 1 sec, the trial was  
319 defined as a correct trial.

320 Since NW arrays generate photocurrent upon UV, blue and green, but not red-light stimulation,  
321 we used red LED to map out the visual field as control. NW arrays were implanted at polar angle of  
322 200 to 250 degrees with eccentricity of 19 and 21 degrees (Fig.7b). The hit rate (number of correct  
323 trials divided by all trials) for red light decreased from 56.7% 5 to 7 weeks after implant surgery to  
324 35.7% in 10 to 12 weeks after implantation. In 14 to 15 weeks after implantation, the hit rate for red  
325 light was 12% (Extended Movie 6). A recent study indicated that subretinal implant of prosthetic  
326 device induced photoreceptor degeneration<sup>17</sup>, consistent with our results. To confirm that Monkey  
327 A was capable of conducting VGS task, the hit rate was more than 80% with red light stimuli ( $642/18$   
328 nm,  $10 \mu\text{W}\cdot\text{mm}^{-2}$ ) in the normal region (Fig.7c, Fig.7e, Extended Data Fig.6c-i, Extended Data Table  
329 2).

330 To examine the NW-arrays-mediated light responses, we used blue and UV LED light to  
331 stimulate the NW-implanted area (Extended Movie 7). Note that the intensity of UV light we used  
332 was lower than that reported for solar light in the late summer afternoon in previous studies and also  
333 much lower than the known damaging thresholds of UV ( $30 \mu\text{W}\cdot\text{mm}^{-2}$ ) for the corneal endothelium,  
334 lens, and retina <sup>48</sup>. The hit rate for blue or UV light was much larger than that for red light 14 ~ 15  
335 weeks after implantation (Fig.7d, Extended Data Table 2). When using red light stimulation, 95.58%  
336 of the endpoints were outside the target area, whereas when stimulating with ultraviolet or blue light,  
337 80.28% of the endpoints located within the target area (Fig.7e-f). The mean hit rates elicited by blue  
338 and UV light were 72.5% and 74% respectively at  $10.00 \mu\text{W}\cdot\text{mm}^{-2}$  (Fig.7g). When the light intensity  
339 was  $1.82 \mu\text{W}\cdot\text{mm}^{-2}$  for blue light or  $0.45 \mu\text{W}\cdot\text{mm}^{-2}$  for UV light, the hit rate fell below 40%. These  
340 results indicated that stimulating NW arrays by blue or UV light-induced saccade behavior in a non-  
341 human primate, rescuing light responses in photoreceptor-degenerated area.

342

## 343 Discussion

344  $\text{TiO}_2$  is one of the most reported inorganic semiconductors, of which the synthesis method  
345 and the working principle have been well established. It possesses the advantages of non-toxic, high  
346 stability and low-cost. In addition, it can enable adsorption for wide-range wavelength light by  
347 tuning the bandgap via Au decoration and oxygen vacancy introduction. In this study, we  
348 demonstrated a NW-array based retinal prosthetic device with high sensitivity. After improving the  
349 fabrication process in the NW arrays from our previous study <sup>26</sup>, the light intensity threshold to elicit  
350 a perceptual response is  $\sim \mu\text{W}\cdot\text{mm}^{-2}$  in both mice and macaque monkey. The intensity of UV light  
351 stimulation in our study was lower than that for solar light in the late summer afternoon and much  
352 lower than the known damage thresholds of UV ( $30 \mu\text{W}\cdot\text{mm}^{-2}$ ) for the corneal endothelium, lens,  
353 and retina <sup>48</sup>. Although a recent study reported activation of retinal and V1 cells in the order of  
354  $\mu\text{W}\cdot\text{mm}^{-2}$  using Channelrhodopsin variant, no behavioral evidence with low irradiance was  
355 presented <sup>50</sup>. Hence, to the best of our knowledge, our NW array is among the state-of-art retinal  
356 prosthetics with very high light sensitivity. Augmentation strategies such as video goggles with light  
357 amplification function <sup>8,53</sup> may further help enhance visual responses in dark environment.

358 One important feature for image-forming vision is spatial resolution. In the clinical trials of

359 subretinal implant alpha-IMS, even though a grating acuity of 3 cpd was reported in one patient, the  
360 majority of patients had low acuity and were not able to read <sup>31</sup>. In a photovoltaic Prima implant,  
361 the restored spatial resolution measured by visually evoked potentials (VEPs) in the visual cortex  
362 was 0.47 cpd in rats <sup>18</sup>. In our study, the NW-array-implanted blind mice were capable of detecting  
363 moving light bars with a spatial resolution of 0.313 cpd. A high-density NW arrays <sup>22</sup> could  
364 potentially pave the way for restored vision with better spatial resolution.

365 Due to the capacitance effect, TiO<sub>2</sub> nanowires exhibit longer durations of photocurrents,  
366 consisted of transient Capacitive current and sustained Faradaic current, than conventional  
367 semiconductors such as silicon (see Extended Data Table 1). In our previous study, we reported both  
368 ON-sustained and ON-transient responses in the RGCs recordings <sup>26</sup>, indicating that ON-sustained  
369 neurons may be responsible for static image perception while ON-transient neurons may be  
370 responsible for image changes (low frequency) and flicker fusion (20 Hz and above). In *in vitro*  
371 experiments in mice, we found that NW arrays elicited reliable responses at 3 Hz and below in ON-  
372 transient RGCs. In behavior experiments, NW-implanted blind mice also exhibited behavioral  
373 responses at 3 Hz and below. These results indicate that NW-array-mediated image-forming vision  
374 enables the perception of slow images changes at 3 Hz, with compensation in flicker fusion.

375 Despite the fact that no chronic inflammation or cell loss was detected in blind mice retina  
376 with NW array implant, saccade experiments in macaque monkeys suggest that in-situ  
377 photoreceptors degenerate at the implant site, which is also observed in other subretinal prosthesis  
378 in primates <sup>53</sup>. For clinical applications, NW array and other subretinal implant are suitable for  
379 patients with complete loss of photoreceptors, including late-stage RP and geographic atrophy <sup>19</sup>.  
380 Moreover, subretinal implants are in principle compatible with optogenetic therapy and other  
381 restoration methods that delays the degeneration of photoreceptors.

382 One intriguing observation from our data is the transiently enhanced responses during the  
383 first week post implant together with continuously improving response reliability in the visual cortex  
384 of blind mice. Interestingly, in the blind patients with Alpha AMS subretinal implant, the  
385 performance in grating detection 3 months after the implant was better than that 2 months after  
386 implant <sup>16</sup>. Together, these results indicated that even in adults who are well beyond the age of the  
387 critical period, the sensory cortex retains certain levels of plasticity, which potentially leads to the  
388 functional rewiring of the visual cortex and improved visual function.

## 389 **Methods**

### 390 **Synthesis of TiO<sub>2-x</sub> NW and Au@TiO<sub>2-x</sub> NW arrays**

391 In a typical synthesis, 0.5 mL tetrabutyl titanate (TBOT) was added into the mixture  
392 solution of 15 mL deionized water and 13 mL hydrochloric acid (HCl). This stirred to form a  
393 transparent solution and fluorine-doped tin oxide (FTO) which coated with hydrophilic surface on  
394 glass substrate were transferred into a 50-mL Teflon-lined stainless-steel autoclave, and heated to  
395 150°C for 12 hours. Then it was annealed at 550°C for 3 hours with a heating rate of 5°C per  
396 minute in the air. This as-synthesized TiO<sub>2</sub> was further annealed under 350 °C in 5% H<sub>2</sub>/Ar  
397 atmosphere for 8 hours, with a flowing rate of 150 ~ 200 standard cubic centimeters per minute  
398 (sccm) to obtain the TiO<sub>2-x</sub> NW arrays with oxygen vacancies. Afterwards, Au nanoparticles were  
399 coated on the TiO<sub>2</sub> NW arrays. In brief, the FTO substrate with TiO<sub>2-x</sub> NWs was immersed into the  
400 0.01 M HAuCl<sub>4</sub> aqueous solution. In such solution, the pH value was tuned to ~ 4.5 by adding 0.2  
401 M NaOH aqueous solution. After incubating for 2 hours, the FTO substrate was taken out, dried and  
402 annealed under 300°C for 2 hours with a heating rate of 5 °C per minute in the Ar atmosphere .  
403 Finally, the FTO substrate was etched at 85°C in a mixed solution of H<sub>2</sub>SO<sub>4</sub>/HF (40 wt%) under the  
404 ratio of 13:2.

405

### 406 **Photocurrent measurement**

407 The photocurrent measurement was carried out using a setup consisting of a Zeiss upright  
408 DIC microscope (Examiner A1, Zeiss, Germany) and a 3-electrode system. The Au@TiO<sub>2-x</sub> NW  
409 arrays photoanode, a coiled Pt wire and an Ag/AgCl were used as working, counter and reference  
410 electrodes, respectively. A phosphate buffer saline (PBS, pH 7.4) was used as the electrolytes. A  
411 glass pipette (resistance within 4.8 ~ 5.2 MΩ) filled with phosphate buffer saline was attached to  
412 the NW arrays and record its photocurrent. Near UV, blue and green light were generated from the  
413 mercury lamp (X-Cite 120, Lumen Dynamics, USA), filtered by fluorescence cubes (UV: 375/28  
414 nm; Blue: 470/20 nm; Green: 546/12 nm, Zeiss Inc., Germany) and proved through the ×40 water-  
415 immersion objective.

416

### 417 **Animals and genotyping**

418 Mice were raised and bred at  $23 \pm 2^{\circ}\text{C}$  room temperature, 60 ~ 65% relative humidity, and a  
419 12 h light/12 h dark cycle. The wild-type (C57BL/6J) mice were purchased from the Slac Laboratory  
420 Animal Co. (Shanghai, China). Homozygous *rd1*<sup>-/-</sup> and cone diphtheria toxin subunit-A (*cone-DTA*)  
421 positive mice (*rd1*<sup>-/-</sup>/*cDTA* mice) were genotyped using protocols described in our previous work <sup>26</sup>.  
422 Details about age were reported in corresponding section of *Results*. The experimental procedures  
423 for mice was approved by the Animal Ethics Committee of School of Basic Medical Sciences at  
424 Fudan University.

425 One male rhesus monkey (*Macaca mulatta*) aging 12 years old and weighing 8 kilograms (in  
426 East China Normal University, Shanghai) was used in this study. The experimental procedures for  
427 macaque monkey was approved by the Institutional Animal Care and Use Committee at East China  
428 Normal University.

429

#### 430 **Patch-clamp recording of retinal ganglion cells in mice retina**

431 Mice were anesthetized with isoflurane (1 ~ 2% at 0.5 ~ 1.0 L/min). Enucleation was  
432 conducted on one eye, which was quickly placed in oxygenated Ringer's solution (in mM, NaCl  
433 124, KCl 2.5, CaCl<sub>2</sub> 2, MgCl<sub>2</sub> 2, NaH<sub>2</sub>PO<sub>4</sub> 1.25, NaHCO<sub>3</sub> 26, and glucose 22, pH 7.35; oxygenated  
434 with 95% O<sub>2</sub> and 5% CO<sub>2</sub>). The retina was dissected and placed on a filter paper (Merck Millipore,  
435 Burlington, USA) in the recording chamber. Subsequently, NW arrays were attached to the inner  
436 nuclear layer of the blind retina. A Glass pipette (resistance: 5 ~ 10 MΩ) was pulled by P-97  
437 micropipette puller (Sutter Instruments, Novato, USA) and filled with internal solution (in mM,  
438 potassium gluconate 105, KCl 5, CaCl<sub>2</sub> 0.5, MgCl<sub>2</sub> 2, EGTA 5, HEPES 10, Mg-ATP 4, GTP-Na  
439 0.5, and sodium phosphocreatine 7, PH = 7.4). An *in vitro* patch clamp system was used to record  
440 action potentials of RGCs using MultiClamp 700B patch-clamp amplifier (Molecular Devices, San  
441 Jose, USA) and digitizer Digidata 1440 (Molecular Devices, San Jose, USA) under DIC microscope  
442 (Zeiss, Oberkochen, Germany) <sup>54</sup>.

443 Visual stimuli were provided by mercury lamp (X-Cite 120PC Q, LUMEN DYNAMICS,  
444 Ontario, Canada) and Digital Micromirror Device (DMD) (wavelength: 400 nm). To investigate the  
445 response of RGCs to light with different wavelengths, UV, blue or green light was presented by  
446 mercury lamp and delivered via a  $\times 40$  water-immersive objective. DMD was used to present  
447 moving, static and flash visual stimuli. The moving light bar appeared at 6.85 degrees/sec for 10

448 times in 30 sec, while static light bar remained on for 30 sec. Different widths of the moving light  
449 bar (0.64, 1.28, 1.92, 2.56, 3.20 and 3.84 degrees) were used to examine the spatial resolution of the  
450 RGCs. Different temporal frequencies (5.00, 2.5, 1.57, 1.25, 1.00 and 0.5 Hz) of flashing stimuli  
451 (area:  $5.76 \times 5.76 \text{ deg}^2$ ) were used to examine the temporal resolution of the RGCs.

452 Clampfit (Axon, Scottsdale, USA) was used to analyze the action potentials of RGCs and  
453 Prism 6 (Graph pad, San Diego, USA) was used to analyze firing rates and fraction of responses.  
454 Firing rate was the number of action potentials during visual stimulation. Fraction of responses was  
455 the number of trials which elicited action potentials divided by 10 (visual stimuli).

456

#### 457 **NW array implant surgery in mice**

458 The *rd1<sup>-/-</sup>/cDTA* mice (blind mice) aged 8 to 10 weeks were anesthetized with isoflurane (1 ~  
459 2% at 0.5 ~ 1.0 L/min). The eye-ball was fixed in a suitable position for implantation by suturing  
460 the upper and lower eyelids. A small incision was made on the dorsal sclera. 1 ~ 2  $\mu\text{L}$  of 0.9%  
461 sodium chloride solution was injected rapidly and carefully with NanoJectII (Drummond Scientific  
462 Company, USA) to induce retinal detachment. The incision was further expanded to make enough  
463 space for the NW array implant, which were inserted carefully into the incision. After the implant,  
464 the suture was removed and the eye-ball was washed with 0.9% saline solution, and applied with  
465 erythromycin eye ointment. The area of NW arrays was 0.5 ~ 1  $\text{mm}^2$  and the NW arrays were  
466 sterilized with autoclave before implanted.

467

#### 468 **Choice-box-based Behavioral Test**

469 The choice-box (240 mm  $\times$  240 mm  $\times$  180 mm) was customized using acrylic sheets,  
470 containing a water delivery system (Kamoer, Shanghai, China, composed of water pipe, water port,  
471 and water pump) and an audio signal system (a buzzer positioned in the middle of the choice-box  
472 lid). Visual stimuli were placed at two positions (12 cm apart). Light intensity of all visual stimuli  
473 in this behavioral task was measured at a distance of 6 cm away from the light source. Visual stimuli,  
474 water delivery system and the audio signal system were all controlled by Arduino.

475 Choice-box-based behavior test was divided into training trials and testing trials<sup>55</sup>. Mice were  
476 water restricted 3 days before the training trials. During the training trials, mice were allowed to  
477 explore the choice box freely for 5 ~ 10 min before the test starts. Trial started by cueing with audio

478 signal (tone 1). After 2 to 3 seconds delay, the visual stimulus appeared randomly at one of the two  
479 visual stimulation locations. The stimulation duration and reaction time are both 20 sec. The mice  
480 were trained to touch the target area (defined by a circle centered at the LED with a diameter of 6  
481 cm in light localization test) associated with the right visual stimuli either by their paws or noses. If  
482 the mice picked the right visual stimuli within the reaction time, another audio signal (tone 2) by  
483 the buzzer will be given and the mice were able to obtain water reward at the water port (defined as  
484 a correct trial). If the mice failed to touch the visual stimulation region within reaction time, the trial  
485 was defined as a miss trial and audio cue and water reward would also not be provided. If the mice  
486 touched area outside the right visual stimuli region on the screen within reaction time, the trial was  
487 defined as a wrong trial and audio cue and water reward would also not be provided. The next trial  
488 would start when the mice stayed away from the visual stimulation region. The interval of each trial  
489 was at least 10 sec, and 40 trials were carried out daily.

490 Testing phase would start when the correct rate of *rd1<sup>-/-</sup>/cDTA* mice implanted with Au@TiO<sub>2</sub>-  
491 <sub>x</sub> NW arrays reached 70% and maintains stability for 3 days. The protocols used in testing phase  
492 was similar to that in the training phase, except that the stimulation duration and the reaction time  
493 were reduced to 10 sec, and the interval between each trial was at least 5 sec.

494 In the light localization test, LED light with different wavelengths and light intensities was  
495 used. LED visual stimuli appeared randomly at one of two visual stimulation locations. In the testing  
496 phase, UV LED light (375/15 nm, 6.24  $\mu\text{W}\cdot\text{mm}^{-2}$ ), blue LED light (465/25 nm, light intensities:  
497 6.75, 3.31, 2.93, 1.53 and 0.64  $\mu\text{W}\cdot\text{mm}^{-2}$ ), and green LED light (535/28 nm, light intensities: 7.83,  
498 4.20, 2.04, and 1.15  $\mu\text{W}\cdot\text{mm}^{-2}$ ) were used.

499 In the experiment of discriminating moving and static light bar, the visual stimulus was  
500 presented by the projector (CB-S41, EPSON, Suwa Japan). A moving light bar stimulus appeared  
501 randomly at one of the two visual stimulation locations, and a static light bar stimulus appeared at  
502 the other position simultaneously. Mice would be rewarded with water if they touched the target  
503 area associated with the moving light bar. In the testing phase, static or moving light bar stimulus  
504 with different widths (widths: 2.63, 3.94, 5.25, 6.57, and 7.88 degrees, velocity: 7.85 degrees/sec)  
505 and velocities (velocities: 5.23, 6.54, 7.85, 9.18, and 10.47 degrees/sec, width: 5.25 degrees) were  
506 used.

507 In the experiment of discriminating flash stimulus and constantly bright stimulus, the visual  
508 stimulus was also presented by the projector (CB-S41, EPSON, Suwa, Japan). A flashing stimulus  
509 (6 cm × 6 cm square) appeared at one of the two positions randomly in the visual stimulation  
510 region, and an ON stimulus appeared at the other position simultaneously. Mice would be rewarded  
511 with water if they touched the target area associated with the flashing stimulus. In the testing phase,  
512 temporal frequencies of 1, 1.25, 2, 3.33 and 5 Hz were used for the flash stimulus.

513

#### 514 **Visual acuity and contrast sensitivity measurement**

515 To measure the visual acuity and contrast sensitivity, we designed a system with 4 LCD  
516 monitors arranged in a quadrangle with a camera installed above the system for video recording.  
517 Visual stimulus (drifting black and white gratings, 12 degree/sec) was generated by Python, using  
518 the Psychopy toolbox <sup>56</sup>. The direction of drifting gratings was switched between clockwise and  
519 counterclockwise. Each direction lasted for 10 sec and repeated for 3 times. One day before testing,  
520 each mouse was habituated staying on the pedestal (height: 12 cm, radius: 4 cm) for several minutes.  
521 On the day of testing, each mouse was placed on the pedestal and allowed to move freely. If the  
522 mouse slipped or jumped off the pedestal, the testing was terminated and resumed.

523 Gray background was presented on the screen at the beginning of each session. When the  
524 mouse stopped moving, the gray background was replaced with drifting grating with the mean  
525 luminance at 100% contrast and the spatial frequency at 0.1 cycle/degree. After unambiguous  
526 tracking behavior was observed, the spatial frequency was increased 0.05 cycle/degree in the next  
527 successive trials until the mouse ceased to track the stimulus. The highest spatial frequency of  
528 drifting grating that the mouse could track was identified as the visual acuity.

529 In contrast sensitivity test, gray background was presented on the screen at the beginning of  
530 each session and was replaced with drifting grating when the mouse stopped moving. The test started  
531 with a grating of 100% contrast at a fixed spatial frequency, and the contrast was reduced by 10%  
532 in each step in the next successive trials until the mouse ceased to track the stimulus, and the contrast  
533 threshold was identified. The contrast threshold was identified at eight spatial frequencies between  
534 0.03 and 0.35 cycle/degree (0.031, 0.045, 0.064, 0.092, 0.130, 0.192, 0.272, 0.350 cycle/degree).

535

#### 536 **Immunohistochemistry**

537 Mice were deeply anesthetized using overdose isoflurane for euthanasia and perfused  
538 transcardially with physiological saline, followed by 4% paraformaldehyde (PFA) using a perfusion  
539 pump. For immunohistochemistry of mic brain, they were kept in 4% PFA for fixation at 4 °C  
540 overnight and then dehydrated in 30% sucrose. After being embedded and frozen, brains tissue was  
541 sectioned into 30- $\mu$ m coronal slices in a cryostat (Leica CM 1950, Leica, Wetzlar, Germany). The  
542 slices were washed with Tris-buffered saline (TBS) 5 times (5 minutes each), covered with  
543 coverslips and mounted to be photograph by a fluorescence microscope (A1R, Nikon, Tokyo, Japan).

544 With regard to immunohistochemistry of mice retina, eyes was enucleated and the retina was  
545 dissected and fixed in 4% PFA for 4 ~ 7 hours at 4 °C. Then the retina was dehydrated using 10%,  
546 20% and 30% sucrose solution respectively. After dehydration, the retina was embedded in optimal  
547 cutting temperature compound (OCT) compound at -80 °C for more than 2 hours, and subsequently  
548 sectioned into 14 mm slices in a cryostat (Leica CM 1950, Leica, Wetzlar, Germany). After rinsed  
549 by TBS and immersed in 0.5% Triton-X-100 for 20 minutes, slices were incubated in a blocking  
550 solution consisting of 10% Donkey serum (Jackson Immunoresearch, USA), 1% bovine serum  
551 albumin (BSA), and 0.05% Triton-X-100 in 0.05 M TBS for 2 hours. Slices were then incubated by  
552 primary antibody (anti-Choline Acetyltransferase and anti-Brn3a, Millipore, Massachusetts, USA,  
553 1:200) diluted in blocking solution overnight. In the following day, slices were washed 3 times (5  
554 minutes each), and secondary antibody (Donkey anti-Goat conjugated to Alexa Flour 594, Jackson  
555 ImmunoResearch, West Grove, USA, 1:300) diluted in blocking solution was used to cover the  
556 slices for 2 hours in darkness. Slices were then stained with 1:3000 DAPI after rinsing, and finally  
557 rinsed, air-dried, and mounted. A fluorescence imaging microscope (A1R, Nikon, Tokyo, Japan)  
558 was used to obtain fluorescence images of the slices. The fluorescence image was then processed  
559 using Adobe Photoshop CC 2018.

560

### 561 **Intravitreal injection in mice**

562 The mice were anesthetized with isoflurane (1 ~ 2% at 0.5 ~ 1.0 L/min). Subsequently, 69 nL  
563 Dil Stain Perchlorate (1.5mg/mL, D282, Invitrogen, USA) was injected into the dorsal nasal retina  
564 of *rd1<sup>-/-</sup>/cDTA* mice, in which the NW arrays were typically implanted, using a Nanoject II  
565 (Drummond scientific company, Broomall, USA). After surgery, mice were placed on a heating pad  
566 to recover and monitored for postoperative health.

567

568 **Virus injection in mice**

569 The mice were first anesthetized with isoflurane (1 ~ 2% at 0.5 ~ 1.0 L/min). Once the animals  
570 lost reflexes, the scalp was shaved and lidocaine applied on the ear bars. Body temperature was  
571 maintained using a heating pad. Sodium hyaluronate eye drops (0.3%, Santen Pharmaceutical Co.,  
572 LTD, Shiga Plant, Japan) were applied to the eyes for protection during surgery. Skin was disinfected  
573 using alternating scrubs of 70% ethanol and betadine and removed to expose the skull. The skull  
574 was scraped to remove connective tissue and to allow adherence later in the procedure. Cranial drill  
575 was used to thin the skull at three injections site (2.1 mm lateral and 3.2 mm posterior, 2.5 mm  
576 lateral and 3.2 mm posterior, 2.3 mm lateral and 3.6 mm posterior of bregma).

577 Glass pipette filled with AAV2/8-hSyn-GCaMP6s (Taitool Bioscience Co., LTD, Shanghai,  
578 China) was inserted to the injection sites using a Nanoject II injector (Drummond Scientific  
579 Company, USA). 40 pulses of 2.3 nL each (92 nL total volume), at 10 seconds intervals, were  
580 delivered to inject the AAV2/8-hSyn-GCaMP6s at the depth of 400  $\mu$ m. The same procedure was  
581 repeated after retracting the pipette to the depth of 320 and 250  $\mu$ m. The pipette was left in the tissue  
582 for 5 minutes before being slowly retracted. Procedures for the stereotaxic injection of the CTB-488  
583 into V1 were the same as described previously.

584

585 **Cranial window implantation in mice**

586 Surgery for cranial window implantation was performed 6 ~ 8 weeks after virus injections  
587 when the mice was over 3.5 ~ 4 months old. Mice were anesthetized with isoflurane (1 ~ 1.5% at 1  
588 ~ 1.5 L/min). Body temperature was maintained using a heating pad. Sodium hyaluronate eye drops  
589 (0.3%) were applied to the eyes for protection during surgery. A ~2.5 mm craniotomy was performed  
590 on the right hemisphere, starting at the 2.3 mm lateral and 1.3 mm anterior of lambda point. The  
591 skull was thinned and soaked in sterile saline solution. Gelfoam (Kang Sen Medical Equipment Co.,  
592 LTD, Guilin, China) soaked in saline was used throughout the procedure to stop bleeding and to  
593 maintain osmosis once the brain was exposed. A custom-made glass window (0.1 mm thickness)  
594 was embedded into the craniotomy and sealed with VetBond (3M Animal Care Products, St. Paul,  
595 USA). Dental cement (Super Bond C&B, Japan) was applied to secured the window. A head bar  
596 was finally mounted on the skull using the same dental cement.

597 Mice were given a dose of ceftiofur sodium (5 mg/kg body weight, Quan Yu Biotechnology  
598 Animal Pharmaceutical Co., LTD, Shanghai, China), dexamethasone sodium phosphate (0.1 mg/kg  
599 body weight, Quanyu Biotechnology Animal Pharmaceutical Co., LTD, Shanghai, China), tolfedine  
600 acid injectable solution (0.1 ml/kg body weight, Vetoquinol, French) and 0.5 ml of sterile saline  
601 towards the end of surgery. Animals were placed in a heated chamber until ambulatory and then  
602 transferred back to their home cage. They were monitored daily for pain and wound health.

603 All mice recovered in home cage for two weeks. Cranial window was examined under a wide  
604 field fluorescence dissection microscope two weeks after cranial window implantation, and  
605 fluorescent labels near the cortical surface should be clearly visible through the wet skull.

606

#### 607 **Procedure for two-photon calcium imaging in mice**

608 Recordings of GCaMP6 fluorescence signals were performed using Olympus FluoView  
609 FVMPE-RS upright two-photon laser-scanning system with an Olympus XL Plan N25 × /1.05 WMP  
610 ∞/0-0.23/FN/18 dipping objective (Olympus, Tokyo, Japan). Two-photon excitation was performed  
611 using 920 nm MAITAI eHPDS-OL laser (Mai Tai, Spectra-Physics, Santa Clara, USA), and emitted  
612 fluorescence was detected through a 495 ~ 540 nm bandpass filter. For the examination of GCaMP6s  
613 expression in V1, cranial window was imaged at a resolution of 512 × 512 pixels at 30 Hz. Imaging  
614 sessions lasted 2 ~ 3 hours including 1 ~ 2 hours of effective imaging time.

615 In light-evoked responses experiments, mice were habituated to head-fixation and running on  
616 the cylindrical treadmill. Once the animals were comfortable with the setup, imaging was performed.  
617 The mice were kept awake during imaging. In receptive field mapping experiments and natural  
618 scenes stimulation experiments, the mice were anesthetized with isoflurane (0.5 ~ 1.0% at 1 ~ 1.5  
619 L/min) and placed on a heating pad to monitor and maintain body temperature. Sodium hyaluronate  
620 eye drops (0.3%) were applied to the eyes to prevent drying.

621

#### 622 **Visual stimulus for two-photon Calcium imaging.**

623 Blue LED was used as light sources for the light-responsive experiments. LED was located 6  
624 cm away from the animal's eye. Each trial started with a blank period for 20 ~ 25 seconds randomly,  
625 and a LED stimulation was subsequently turned on for 1 sec and repeated for 6 times.

626 Stimulus used in receptive field mapping was generated by Python, using the Psychopy toolbox

627 <sup>56</sup>. The screen was adjusted to be 45 degrees from the anteroposterior axis, 12 cm from the animal's  
628 eye, subtending 96 and 80 degrees of the horizontal and vertical visual field, respectively. We used  
629 a sparse noise stimulus, consisting of blue squares presented on a black background along a grid of  
630  $6 \times 5$  squares to map RFs, each square is  $\sim 16 \times 16$  degrees. The squares were presented for 1 sec  
631 with a 10 sec interval with 8 repetitions for anesthetized mice.

632 Stimuli of natural scenes were consisted of 30 natural images from the van Hateren Natural  
633 Image Dataset <sup>61</sup> and the McGill Calibrated Colour Image Database <sup>62</sup>. The images of  $800 \times 600$   
634 pixels were presented in grayscale with normalized contrast. Each image was presented for 0.5 sec  
635 followed by 5 sec inter-image gray period and repeated for 4 ~ 8 times.

636

### 637 **Analysis of *in vivo* calcium imaging data**

638 *In vivo* calcium movies were pre-processed in python using a custom-built pipeline based on  
639 CaImAn package <sup>63</sup> for large-scale calcium imaging data analysis. Movies were motion-corrected  
640 using a rigid registration method to remove motion artifacts <sup>64</sup>. Fluorescence traces of individual  
641 neurons were extracted from the registered movie using a constrained non-negative matrix  
642 factorization (CNMF) framework <sup>65</sup>. Spatial correlation thresholds for ROI detection were set to  
643 0.85, and the signal to noise ratio for accepting a component was set to 2.50. The automatic detection  
644 was manually screened to ensure correct segmentation of somatic calcium activity. This pipeline  
645 generated a set of spatial footprints and temporal traces for each animal on each day of recording.  
646 The changes in fluorescence ( $\Delta F/F$ ) trace and z-score were used in further analyses.

647

### 648 **Identification of light-responsive neurons**

649 To identify light-responsive neurons, we defined a pre-stimulus period as the 2-sec window (60  
650 frames) preceding the stimulus onset, and the baseline of the trial was the mean  $\Delta F/F$  during the  
651 pre-stimulus period. We also defined a post-stimulus period as the 5-sec window (150 frames)  
652 following the stimulus onset. Post-stimulus window was 1 sec in the natural scenes stimulus  
653 experiments. A neuron was considered responsive to the 1-sec light pulses if the maximum  $\Delta F/F$   
654 during the post-stimulus period was more than 5 times SD above the baseline and the time to decay  
655 half-peak must be over 10 frames in more than 50% of the trials. In the natural scenes test, the  
656 neuron which satisfied the above conditions would be identified as responsive cells for further

657 analysis.

658

### 659 **Mean $\Delta F/F$ amplitude and latency in V1 neurons**

660 To estimate an ROI's  $\Delta F/F$  mean amplitude in response to light stimuli, we segmented the  $\Delta F/F$   
661 traces during each light-evoked spiking and used the maximum  $\Delta F/F$  value at each segment as a  
662 measurement of the  $\Delta F/F$  amplitude for that particular segment. The time difference between the  
663 onset of the visual stimuli and the frame at which the  $\Delta F/F$  trace first exceeded the threshold was  
664 defined as the latency. The average of these maximal values and latencies for light-responsive  
665 neurons were computed as the mean  $\Delta F/F$  and latency, respectively. The latency was normalized by  
666 the average latency in normal mice. The mean  $\Delta F/F$  was normalized by the  $\Delta F/F$  amplitude at the  
667 3rd day after implantation.

668

### 669 **Fitting spatial receptive fields in V1 neurons in mice**

670 The retinotopic organization of individual neurons was assessed by measuring the average  
671  $\Delta F/F$  response to each of the 30 stimulus positions ( $6 \times 5$  grid) with 8 repetitions. These data were  
672 interpolated by a 2D bilinear interpolation, and fit by least-squares regression with a two-  
673 dimensional Gaussian Model. Neurons whose receptive field (center) was positioned 5 degrees from  
674 the edge of the screen (that provide visual stimuli) were chosen for further analysis.

675

### 676 **Lifetime sparseness.**

677 Lifetime sparseness was computed from the mean responses to natural scenes by using the  
678 definition in previous study<sup>43,46</sup>, as

$$679 \quad S_L = \frac{1 - \frac{1}{N} \frac{(\sum_i r_i)^2}{\sum_i r_i^2}}{1 - \frac{1}{N}}$$

680 where  $N$  is the number of stimulus conditions and  $r_i$  is the mean response to stimulus condition  
681  $i$  across the test.

682

### 683 **Surgical procedures for NW arrays implantation in macaque monkey**

684 Macaque monkey was anesthetized with intramuscular tiletamine hydrochloride and

685 zolazepam hydrochloride (Zoletil 50, 0.1 mL/kg body weight, Virbac S.A., France) 20 minutes after  
686 intramuscular atropine (0.5 mg/mL, 0.1 mL/kg body weight, Heulton Animal Pharmaceutical Co.,  
687 LTD, Sichuan, China). Isoflurane inhalation maintained general anesthesia during retinal implant  
688 surgery. Mydriasis in the right eye was induced by tropicamide (5 mg/mL, Santen  
689 Pharmaceutical Co., LTD, Osaka, Japan). Lateral canthotomy was performed to allow 23-gauge  
690 trocars (Carl Zeiss Meditec AG, Jena, Germany) for vitrectomy and a retinal bleb was created by  
691 subretinal injection of balanced salt solution<sup>17</sup>. NW arrays were 1.8 mm in length and 0.4 mm in  
692 width, so as to be guided into the eyes through 23-gauge trocars for vitrectomy without an additional  
693 incision, reducing potential infections and post-surgery complications. 8 pieces of implantation in  
694 all were inserted subretinally through 3 mm-wide sclerotomies in Monkey A (Constellation vision  
695 system, Fort Worth, USA). The detached retina was reattached by perfluorocarbon liquid (Bausch  
696 & Lomb, Rochester, USA) and silicone oil (Arciolane3000, Arcadophta SARL, France). Retinal  
697 laser photocoagulation was operated at the border of the retinotomy<sup>66,67</sup>.

698

#### 699 **Eyes Examinations for macaque monkey**

700 One to two drops of Compound Tropicamide Eye Drops (Santen Pharmaceutical Co., LTD,  
701 Shiga Plant, Japan) were instilled into Monkey A's eyes to dilute its pupil 3 times and 1 hour before  
702 the examination began. Monkey A was injected with atropine (0.5 mg/mL, 0.1 mL/kg body weight,  
703 Heulton Animal Pharmaceutical Co., LTD, Sichuan, China) followed by intramuscular injection of  
704 tiletamine hydrochloride and zolazepam hydrochloride (Zoletil 50, 0.1 mL/kg body weight, Virbac  
705 S.A., France). After anesthetization, Monkey A was placed prone in a supporting apparatus to  
706 receive eye examinations.

707 Color, Red-free, and autofluorescence fundus photography (TRC-50DX, TOPCON, Tokyo,  
708 Japan) of Monkey A's right eye were taken before photocoagulation, 11 months after  
709 photocoagulation, 4 days, 3, 4, 6 and 8 weeks after NW arrays implantation. Optic Coherence  
710 Tomography (OCT) (Cirrus HD-OCT 4000, Zeiss, Oberkochen Germany) was used to scan the  
711 retinal structure and the corresponding places of NW arrays. OCT images were taken at 4 days, 3,  
712 4, 6 and 8 weeks after implantation with NW arrays. Silt lamp (Oculus Optikgerate GmbH, Wetzlar,  
713 Germany) was used to examine Monkey A's lenses, cornea and anterior chamber by providing direct  
714 visualization.

715

716 **Recording of eye position and visually-guided saccade task in macaque monkey**

717 Monkey A was seated in a chair which was placed on a platform in front of the screen (the  
718 distance between the monkey's eyes and the screen is 30 cm) and looked flat at the central fixation  
719 point. A lightweight acrylic cap was implanted for head stabilization chronically. Monkey A's head  
720 was fixed by a custom-made head holder to keep the head stable during experiment. Pupil position  
721 was monitored and digitalized by an infrared eye system, including an eye-tracking camera (above  
722 the center of the screen), infrared illuminator, Eyelink plus 1000 (SR Research, USA) and Wise  
723 center software (Jisimingzhi Technology Co., Ltd. Beijing, China).

724 Visual stimuli were presented by red (642/18 nm), blue (465/25 nm) or UV (360/15 nm) LED,  
725 which were generated by TEMPO experiment control system (Reflective computing, Olympia, WA,  
726 USA), Neurotask software (SourceForge, San Diego, USA) and Arduino. Monkey A's eye in  
727 visually-guided saccade task was 30 cm away from the stimulus. The light intensity of the stimulus  
728 (red (642/18 nm), blue (465/25 nm) or UV (360/15 nm) LED) was set to  $\sim 10.00 \mu\text{W}\cdot\text{mm}^{-2}$  by an  
729 electric current source (DP3005B, MESTEK, Shenzhen, China) at a distance of 30 cm from the  
730 stimulus. We also measured the light intensity at a distance of 6 cm ( $\sim 107.00 \mu\text{W}\cdot\text{mm}^{-2}$ ) from the  
731 same stimulus to ensure consistency with mice experiment.

732 The monkey was trained daily to perform a visually-guided saccade task and was rewarded for  
733 making saccadic eye movement from a central fixation point (equipped with an LED) to a peripheral  
734 target point (equipped with an LED). In each session, stimulations were presented in the implanted  
735 region and more than 4 normal regions in a random order. Up to ten sessions were recorded daily.  
736 Once Monkey A fixated at the fixation point for 1 sec, the LED at the target point was turned on for  
737 1 sec while the LED at the fixation point was turned off. The visual field was divided into 36 polar  
738 angles, with eccentricity from 17 to 21 degrees (interval 2 degrees).

739 To calculate the saccadic endpoint, we measured the velocity of eye movement trajectories  
740 using customized python code. The saccadic endpoint was the average position in the time window  
741 when the eye was first stationary for 50 ~ 100 milliseconds after peak velocity<sup>21</sup>. The experiment  
742 animal was considered to have completed one correct saccade when the animal gaze reached a 15°  
743 window surrounding the target point and maintained more than 50 milliseconds. The animal was  
744 rewarded when it made a correct saccadic eye movement. Each saccadic endpoint was normalized

745 according to the relative position of the target point.

746

#### 747 **Statistical analysis**

748 The differences and normality for multiple comparisons were tested by Prism (Graphpad, San  
749 Diego, CA). Comparisons between two distinct samples were made by two-tailed Student's  
750 unpaired t-test, and paired t-test were used for data with repeated measurements from the same  
751 sample. Comparisons between three or more distinct samples were made by one-way ANOVA  
752 followed by the Tukey post-hoc test. Results of the choice-box-based behavioral test were analyzed  
753 by two-way repeated-measures (RM) ANOVA followed by the Tukey post-hoc test. Results of  
754 patch-clamp recording and visually-guided saccade test were analyzed by one-way repeated-  
755 measures ANOVA followed by the Dunnett post-hoc test. With regards to the fitting model, we  
756 used log-linear regression to fit the data.  $P < 0.05$  was considered statistically significant. Data are  
757 presented as mean  $\pm$  SEM. Full statistical analyses corresponding to each figure can be found in  
758 Extended Data Table 3.

759

#### 760 **Data availability**

761 Data used from this study are available from the corresponding author upon request.

762

#### 763 **Code availability**

764 Custom-written codes used to analyze data from this study are available from the  
765 corresponding author upon request.

766

#### 767 **References**

- 768 1 Maguire, A. M. *et al.* Safety and efficacy of gene transfer for Leber's congenital amaurosis.  
769 *The New England journal of medicine* **358**, 2240-2248, doi:10.1056/NEJMoa0802315  
770 (2008).
- 771 2 Cascella, R. *et al.* Towards the application of precision medicine in Age-Related Macular  
772 Degeneration. *Progress in retinal and eye research* **63**, 132-146,  
773 doi:10.1016/j.preteyeres.2017.11.004 (2018).
- 774 3 Zhou, H. *et al.* Glia-to-Neuron Conversion by CRISPR-CasRx Alleviates Symptoms of  
775 Neurological Disease in Mice. *Cell* **181**, 590-603.e516, doi:10.1016/j.cell.2020.03.024  
776 (2020).
- 777 4 Mahato, B. *et al.* Pharmacologic fibroblast reprogramming into photoreceptors restores

778 vision. *Nature* **581**, 83-88, doi:10.1038/s41586-020-2201-4 (2020).

779 5 Hoang, T. *et al.* Gene regulatory networks controlling vertebrate retinal regeneration.  
780 *Science (New York, N.Y.)* **370**, doi:10.1126/science.abb8598 (2020).

781 6 Lu, Y. *et al.* Reprogramming to recover youthful epigenetic information and restore vision.  
782 *Nature* **588**, 124-129, doi:10.1038/s41586-020-2975-4 (2020).

783 7 Maeder, M. L. *et al.* Development of a gene-editing approach to restore vision loss in  
784 Leber congenital amaurosis type 10. *Nature medicine* **25**, 229-233, doi:10.1038/s41591-  
785 018-0327-9 (2019).

786 8 Sahel, J. A. *et al.* Partial recovery of visual function in a blind patient after optogenetic  
787 therapy. *Nature medicine* **27**, 1223-1229, doi:10.1038/s41591-021-01351-4 (2021).

788 9 Roska, B. & Sahel, J. A. Restoring vision. *Nature* **557**, 359-367, doi:10.1038/s41586-018-  
789 0076-4 (2018).

790 10 Sahel, J. A., Bennett, J. & Roska, B. Depicting brighter possibilities for treating blindness.  
791 *Science translational medicine* **11**, doi:10.1126/scitranslmed.aax2324 (2019).

792 11 Humayun, M. S. *et al.* Visual perception elicited by electrical stimulation of retina in blind  
793 humans. *Archives of ophthalmology (Chicago, Ill. : 1960)* **114**, 40-46,  
794 doi:10.1001/archophth.1996.01100130038006 (1996).

795 12 da Cruz, L. *et al.* Five-Year Safety and Performance Results from the Argus II Retinal  
796 Prosthesis System Clinical Trial. *Ophthalmology* **123**, 2248-2254,  
797 doi:10.1016/j.ophtha.2016.06.049 (2016).

798 13 Wilke, R. *et al.* Spatial resolution and perception of patterns mediated by a subretinal 16-  
799 electrode array in patients blinded by hereditary retinal dystrophies. *Investigative*  
800 *ophthalmology & visual science* **52**, 5995-6003, doi:10.1167/iovs.10-6946 (2011).

801 14 Mills, J. O., Jalil, A. & Stanga, P. E. Electronic retinal implants and artificial vision: journey  
802 and present. *Eye (London, England)* **31**, 1383-1398, doi:10.1038/eye.2017.65 (2017).

803 15 Stingl, K. *et al.* Interim Results of a Multicenter Trial with the New Electronic Subretinal  
804 Implant Alpha AMS in 15 Patients Blind from Inherited Retinal Degenerations. *Frontiers in*  
805 *neuroscience* **11**, 445, doi:10.3389/fnins.2017.00445 (2017).

806 16 Edwards, T. L. *et al.* Assessment of the Electronic Retinal Implant Alpha AMS in Restoring  
807 Vision to Blind Patients with End-Stage Retinitis Pigmentosa. *Ophthalmology* **125**, 432-  
808 443, doi:10.1016/j.ophtha.2017.09.019 (2018).

809 17 Prevot, P. H. *et al.* Behavioural responses to a photovoltaic subretinal prosthesis implanted  
810 in non-human primates. *Nature biomedical engineering* **4**, 172-180, doi:10.1038/s41551-  
811 019-0484-2 (2020).

812 18 Lorach, H. *et al.* Photovoltaic restoration of sight with high visual acuity. *Nat Med* **21**, 476-  
813 482, doi:10.1038/nm.3851 (2015).

814 19 Palanker, D., Le Mer, Y., Mohand-Said, S., Muqit, M. & Sahel, J. A. Photovoltaic Restoration  
815 of Central Vision in Atrophic Age-Related Macular Degeneration. *Ophthalmology* **127**,  
816 1097-1104, doi:10.1016/j.ophtha.2020.02.024 (2020).

817 20 Beauchamp, M. S. *et al.* Dynamic Stimulation of Visual Cortex Produces Form Vision in  
818 Sighted and Blind Humans. *Cell* **181**, 774-783 e775, doi:10.1016/j.cell.2020.04.033 (2020).

819 21 Chen, X., Wang, F., Fernandez, E. & Roelfsema, P. R. Shape perception via a high-channel-  
820 count neuroprosthesis in monkey visual cortex. *Science* **370**, 1191-1196,  
821 doi:10.1126/science.abd7435 (2020).

- 822 22 Gu, L. *et al.* A biomimetic eye with a hemispherical perovskite nanowire array retina.  
823 *Nature* **581**, 278-282, doi:10.1038/s41586-020-2285-x (2020).
- 824 23 Nelidova, D. *et al.* Restoring light sensitivity using tunable near-infrared sensors. *Science*  
825 **368**, 1108-1113, doi:10.1126/science.aaz5887 (2020).
- 826 24 Maya-Vetencourt, J. F. *et al.* Subretinally injected semiconducting polymer nanoparticles  
827 rescue vision in a rat model of retinal dystrophy. *Nat Nanotechnol* **15**, 698-708,  
828 doi:10.1038/s41565-020-0696-3 (2020).
- 829 25 Acaron Ledesma, H. *et al.* An atlas of nano-enabled neural interfaces. *Nat Nanotechnol*  
830 **14**, 645-657, doi:10.1038/s41565-019-0487-x (2019).
- 831 26 Tang, J. *et al.* Nanowire arrays restore vision in blind mice. *Nat Commun* **9**, 786,  
832 doi:10.1038/s41467-018-03212-0 (2018).
- 833 27 Li, J. *et al.* Nanoscale stacking fault-assisted room temperature plasticity in flash-sintered  
834 TiO<sub>2</sub>. *Science advances* **5**, eaaw5519, doi:10.1126/sciadv.aaw5519 (2019).
- 835 28 Wang, G., Wang, H., Ling, Y., Tang, Y. & Li, Y. Hydrogen-Treated TiO<sub>2</sub> Nanowire Arrays  
836 for Photoelectrochemical Water Splitting. *Nano letters* **11**, 3026-3033 (2011).
- 837 29 Jiang, Y. *et al.* Rational design of silicon structures for optically controlled multiscale  
838 biointerfaces. *Nature biomedical engineering* **2**, 508-521, doi:10.1038/s41551-018-  
839 0230-1 (2018).
- 840 30 Geruschat, D. R. *et al.* An analysis of observer-rated functional vision in patients implanted  
841 with the Argus II Retinal Prosthesis System at three years. *Clinical & experimental*  
842 *optometry* **99**, 227-232, doi:10.1111/cxo.12359 (2016).
- 843 31 Stingl, K. *et al.* Artificial vision with wirelessly powered subretinal electronic implant alpha-  
844 IMS. *Proceedings. Biological sciences* **280**, 20130077, doi:10.1098/rspb.2013.0077 (2013).
- 845 32 Spitschan, M. Melanopsin contributions to non-visual and visual function. *Curr Opin*  
846 *Behav Sci* **30**, 67-72, doi:10.1016/j.cobeha.2019.06.004 (2019).
- 847 33 Stingl, K. *et al.* Subretinal Visual Implant Alpha IMS--Clinical trial interim report. *Vision Res*  
848 **111**, 149-160, doi:10.1016/j.visres.2015.03.001 (2015).
- 849 34 Humayun, M. S. *et al.* Interim results from the international trial of Second Sight's visual  
850 prosthesis. *Ophthalmology* **119**, 779-788, doi:10.1016/j.ophtha.2011.09.028 (2012).
- 851 35 Xiong, Y.-Z. *et al.* Relationship Between Acuity and Contrast Sensitivity: Differences Due  
852 to Eye Disease. *Investigative ophthalmology & visual science* **61**, 40-40,  
853 doi:10.1167/iovs.61.6.40 (2020).
- 854 36 Ganjawala, T. H., Lu, Q., Fenner, M. D., Abrams, G. W. & Pan, Z. H. Improved CoChR  
855 Variants Restore Visual Acuity and Contrast Sensitivity in a Mouse Model of Blindness  
856 under Ambient Light Conditions. *Mol Ther* **27**, 1195-1205,  
857 doi:10.1016/j.ymthe.2019.04.002 (2019).
- 858 37 Prusky, G. T., Alam, N. M., Beekman, S. & Douglas, R. M. Rapid Quantification of Adult and  
859 Developing Mouse Spatial Vision Using a Virtual Optomotor System. *Investigative*  
860 *ophthalmology & visual science* **45**, 4611-4616, doi:10.1167/iovs.04-0541 (2004).
- 861 38 Harvey, B. M. & Dumoulin, S. O. The relationship between cortical magnification factor  
862 and population receptive field size in human visual cortex: constancies in cortical  
863 architecture. *The Journal of neuroscience : the official journal of the Society for*  
864 *Neuroscience* **31**, 13604-13612, doi:10.1523/JNEUROSCI.2572-11.2011 (2011).
- 865 39 Wang, Q. & Burkhalter, A. Area map of mouse visual cortex. *The Journal of comparative*

866 *neurology* **502**, 339-357, doi:10.1002/cne.21286 (2007).

867 40 Sterratt, D. C., Lyngholm, D., Willshaw, D. J. & Thompson, I. D. Standard anatomical and  
868 visual space for the mouse retina: computational reconstruction and transformation of  
869 flattened retinæ with the Retistruct package. *PLoS computational biology* **9**, e1002921,  
870 doi:10.1371/journal.pcbi.1002921 (2013).

871 41 Roth, M. M. *et al.* Thalamic nuclei convey diverse contextual information to layer 1 of visual  
872 cortex. *Nature neuroscience* **19**, 299-307, doi:10.1038/nn.4197 (2016).

873 42 Samonds, J. M., Feese, B. D., Lee, T. S. & Kuhlman, S. J. Nonuniform surround suppression  
874 of visual responses in mouse V1. *Journal of neurophysiology* **118**, 3282-3292,  
875 doi:10.1152/jn.00172.2017 (2017).

876 43 Vinje, W. E. & Gallant, J. L. Sparse coding and decorrelation in primary visual cortex during  
877 natural vision. *Science (New York, N.Y.)* **287**, 1273-1276,  
878 doi:10.1126/science.287.5456.1273 (2000).

879 44 Yoshida, T. & Ohki, K. Natural images are reliably represented by sparse and variable  
880 populations of neurons in visual cortex. *Nature communications* **11**, 872,  
881 doi:10.1038/s41467-020-14645-x (2020).

882 45 Rolls, E. T. & Tovee, M. J. Sparseness of the neuronal representation of stimuli in the  
883 primate temporal visual cortex. *Journal of neurophysiology* **73**, 713-726,  
884 doi:10.1152/jn.1995.73.2.713 (1995).

885 46 de Vries, S. E. J. *et al.* A large-scale standardized physiological survey reveals functional  
886 organization of the mouse visual cortex. *Nature neuroscience* **23**, 138-151,  
887 doi:10.1038/s41593-019-0550-9 (2020).

888 47 Kalia, A. *et al.* Development of pattern vision following early and extended blindness.  
889 *Proceedings of the National Academy of Sciences of the United States of America* **111**,  
890 2035-2039, doi:10.1073/pnas.1311041111 (2014).

891 48 Spoerl, E., Mrochen, M., Sliney, D., Trokel, S. & Seiler, T. Safety of UVA-riboflavin cross-  
892 linking of the cornea. *Cornea* **26**, 385-389, doi:10.1097/ICO.0b013e3180334f78 (2007).

893 49 Marie, M. *et al.* Phototoxic damage to cone photoreceptors can be independent of the  
894 visual pigment: the porphyrin hypothesis. *Cell Death Dis* **11**, 711, doi:10.1038/s41419-  
895 020-02918-8 (2020).

896 50 Watanabe, Y. *et al.* Development of an optogenetic gene sensitive to daylight and its  
897 implications in vision restoration. *NPJ Regen Med* **6**, 64, doi:10.1038/s41536-021-00177-  
898 5 (2021).

899 51 Markmann, S. *et al.* Biology of the Adrenal Gland Cortex Obviates Effective Use of Adeno-  
900 Associated Virus Vectors to Treat Hereditary Adrenal Disorders. *Hum Gene Ther* **29**, 403-  
901 412, doi:10.1089/hum.2017.203 (2018).

902 52 Keiser, M. S. *et al.* Toxicity after AAV delivery of RNAi expression constructs into nonhuman  
903 primate brain. *Nature medicine* **27**, 1982-1989, doi:10.1038/s41591-021-01522-3 (2021).

904 53 Prévot, P. H. *et al.* Behavioural responses to a photovoltaic subretinal prosthesis implanted  
905 in non-human primates. *Nature biomedical engineering* **4**, 172-180, doi:10.1038/s41551-  
906 019-0484-2 (2020).

907 54 Boinagrov, D. *et al.* Upper threshold of extracellular neural stimulation. *Journal of*  
908 *neurophysiology* **108**, 3233-3238, doi:10.1152/jn.01058.2011 (2012).

909 55 Li, X. *et al.* Serotonin receptor 2c-expressing cells in the ventral CA1 control attention via

910 innervation of the Edinger-Westphal nucleus. *Nature neuroscience* **21**, 1239-1250,  
911 doi:10.1038/s41593-018-0207-0 (2018).

912 56 Peirce, J. W. PsychoPy--Psychophysics software in Python. *Journal of neuroscience*  
913 *methods* **162**, 8-13, doi:10.1016/j.jneumeth.2006.11.017 (2007).

914 57 Fang, Q. *et al.* A Differential Circuit via Retino-Colliculo-Pulvinar Pathway Enhances  
915 Feature Selectivity in Visual Cortex through Surround Suppression. *Neuron* **105**, 355-  
916 369.e356, doi:10.1016/j.neuron.2019.10.027 (2020).

917 58 Carrillo-Reid, L., Han, S., Yang, W., Akrouh, A. & Yuste, R. Controlling Visually Guided  
918 Behavior by Holographic Recalling of Cortical Ensembles. *Cell* **178**, 447-457.e445,  
919 doi:10.1016/j.cell.2019.05.045 (2019).

920 59 Rossi, L. F., Harris, K. D. & Carandini, M. Spatial connectivity matches direction selectivity  
921 in visual cortex. *Nature* **588**, 648-652, doi:10.1038/s41586-020-2894-4 (2020).

922 60 Rasmussen, R., Matsumoto, A., Dahlstrup Sietam, M. & Yonehara, K. A segregated cortical  
923 stream for retinal direction selectivity. *Nature communications* **11**, 831,  
924 doi:10.1038/s41467-020-14643-z (2020).

925 61 van Hateren, J. H. & van der Schaaf, A. Independent component filters of natural images  
926 compared with simple cells in primary visual cortex. *Proceedings. Biological sciences* **265**,  
927 359-366, doi:10.1098/rspb.1998.0303 (1998).

928 62 Olmos, A. & Kingdom, F. A. A biologically inspired algorithm for the recovery of shading  
929 and reflectance images. *Perception* **33**, 1463-1473, doi:10.1068/p5321 (2004).

930 63 Giovannucci, A. *et al.* CalmAn an open source tool for scalable calcium imaging data  
931 analysis. *eLife* **8**, doi:10.7554/eLife.38173 (2019).

932 64 Pnevmatikakis, E. A. & Giovannucci, A. NoRMCorre: An online algorithm for piecewise  
933 rigid motion correction of calcium imaging data. *Journal of neuroscience methods* **291**,  
934 83-94, doi:10.1016/j.jneumeth.2017.07.031 (2017).

935 65 Pnevmatikakis, E. A. *et al.* Simultaneous Denoising, Deconvolution, and Demixing of  
936 Calcium Imaging Data. *Neuron* **89**, 285-299, doi:10.1016/j.neuron.2015.11.037 (2016).

937 66 Matsuo, T. *et al.* Visual Evoked Potential Recovery by Subretinal Implantation of  
938 Photoelectric Dye-Coupled Thin Film Retinal Prosthesis in Monkey Eyes With Macular  
939 Degeneration. *Artificial organs* **42**, E186-e203, doi:10.1111/aor.13120 (2018).

940 67 Tu, H. Y. *et al.* Medium- to long-term survival and functional examination of human iPSC-  
941 derived retinas in rat and primate models of retinal degeneration. *EBioMedicine* **39**, 562-  
942 574, doi:10.1016/j.ebiom.2018.11.028 (2019).

943 68 Yang, Y., da Costa, R. C., Fuchter, M. J. & Campbell, A. J. Circularly polarized light detection  
944 by a chiral organic semiconductor transistor. *Nature photonics* **7**, 634-638,  
945 doi:10.1038/nphoton.2013.176 (2013).

946 69 van de Burgt, Y. *et al.* A non-volatile organic electrochemical device as a low-voltage  
947 artificial synapse for neuromorphic computing. *Nature materials* **16**, 414-418,  
948 doi:10.1038/nmat4856 (2017).

949 70 Hu, Q. *et al.* Conjugation of haematopoietic stem cells and platelets decorated with anti-  
950 PD-1 antibodies augments anti-leukaemia efficacy. *Nature biomedical engineering* **2**,  
951 831-840, doi:10.1038/s41551-018-0310-2 (2018).

952

953 **Acknowledgments** The authors thank the following funding agencies for supporting this work: the

954 NSF of China (31771195, 81790640, 82021002, 82071200, 22025502), a Shanghai Municipal  
955 Science and Technology Major Project (2018SHZDZX01), ZJLab and Shanghai Center for Brain  
956 Science and Brain-Inspired Technology, Key Scientific Technological Innovation Research Project  
957 of the Ministry of Education, Sanming Project of Medicine in Shenzhen (SZSM202011015),  
958 Shanghai Hospital Development Center (SHDC2020CR4007), Shanghai Health and Family  
959 Planning Commission (20164Y0096, 20184Y0184), Research and Development Fund of  
960 Zhongshan Hospital (2020ZSFZ19).

961

962 **Author contributions** J.Z., B.Y. and Y. Y. conceived the study. J.Z. and B.Y. wrote the paper. R. Y.  
963 performed the behavioral experiments of mice and monkeys, refined the techniques, and analyzed  
964 the data, with help from P.Z., K.S., L.F., R.M.. T. Z., C.P. and G.Z. synthesized the Au@TiO<sub>2-x</sub> NW  
965 arrays. P.Z., R.Y. and Y.C. developed two-photon microscope setups and chronic calcium imaging.  
966 Z.W., S.W. and G.W. performed *in vitro* patch clamp experiments. L.W., M.S., C.D., F.Y. and Y.Y.  
967 conducted the surgical procedures for NW arrays implantation in monkey. C.F., Y.Z., A.C., and F.Z.  
968 worked on monkeys' eyes examinations. S.J., W.X. and F.W. worked on choice-box-based  
969 behavioral device assembly. All authors discussed the results and commented on the manuscript.

970

#### 971 **Competing interests**

972 The authors declare no competing interests.

#### 973 **Additional information**

974 **Correspondence and requests for materials** should be addressed to J.Z., B.Y., or Y.Y.

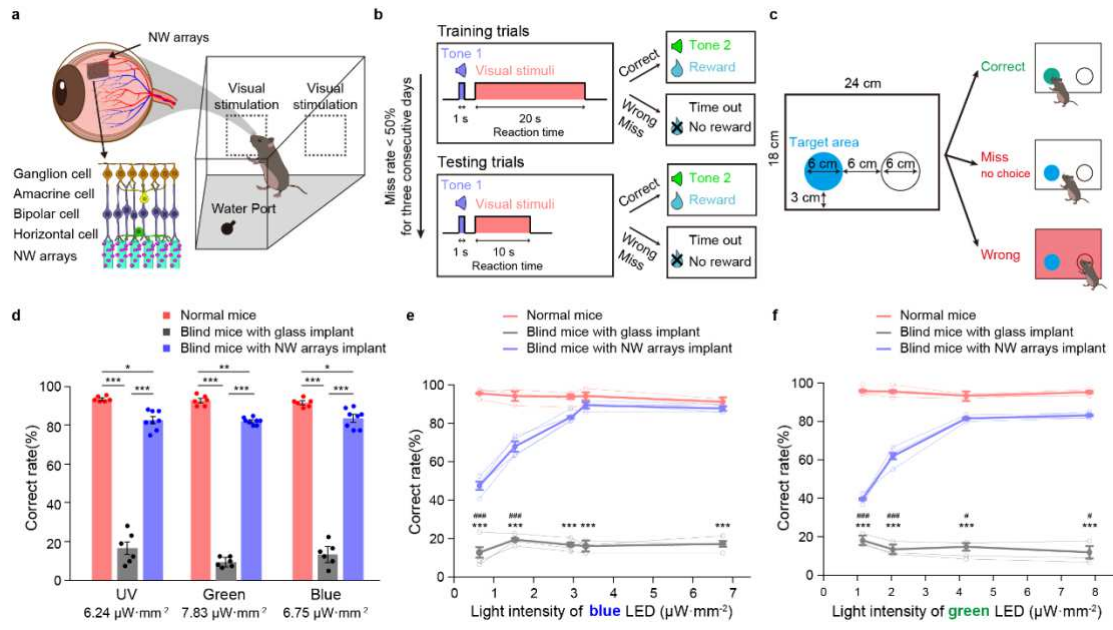
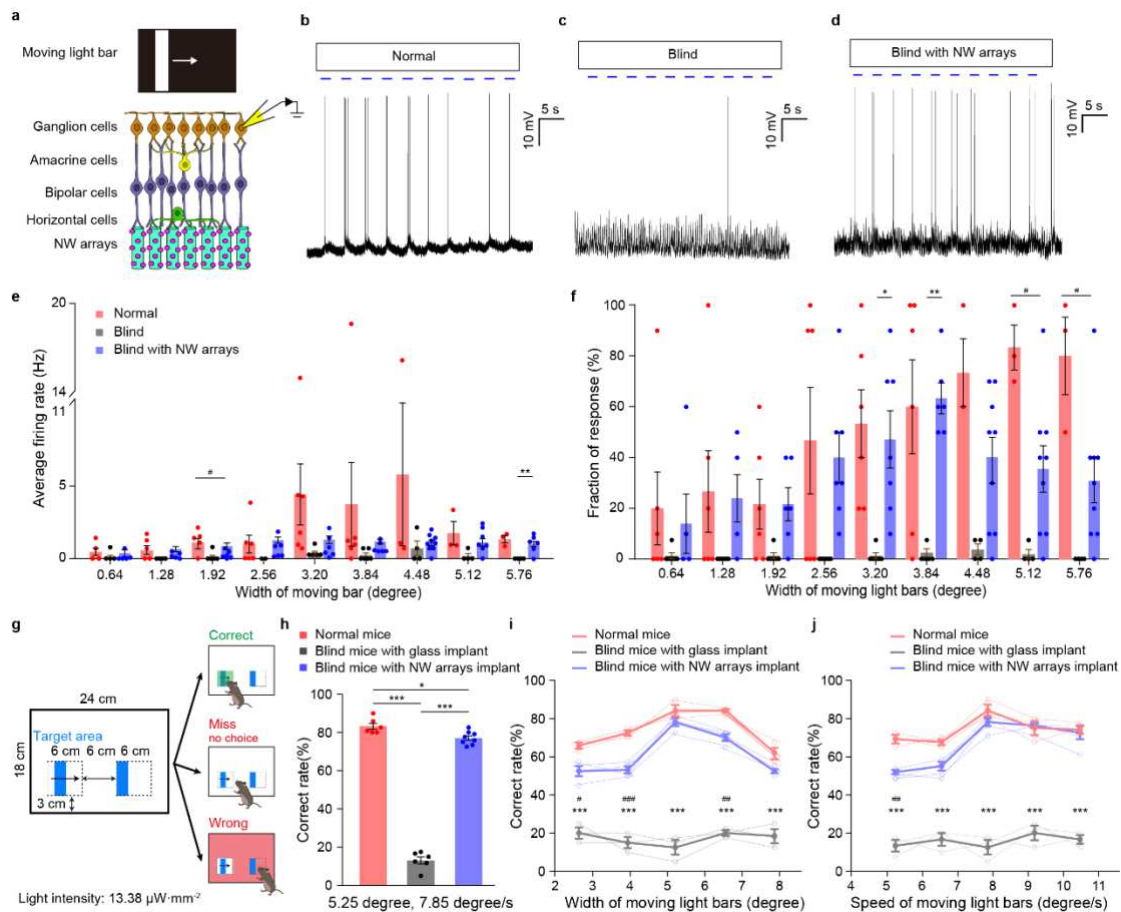


**Fig. 1 | Choice-box-based behavioral paradigm and light localization test.**

**a**, Schematics of Au@TiO<sub>2-x</sub> NW arrays implanted blind mice in a choice-box-based behavioral system. **b**, Behavioral paradigm for the choice-box-based test. **c**, Schematics of light localization test. Two LEDs of the same color were presented. Target area was defined by a circle centered at the LED with a diameter of 6 cm. **d**, Correct rate of normal mice (n = 6), blind mice with glass implant (n = 6) and blind mice with NW arrays implant (n = 8) with UV (375/15 nm, 6.24 μW·mm<sup>-2</sup>), green (535/28 nm, 7.83 μW·mm<sup>-2</sup>) and blue LEDs (465/25 nm, 6.75 μW·mm<sup>-2</sup>). **e-f**, Correct rate of normal mice (n = 3), blind mice with glass implant (n = 3) and blind mice with NW arrays implant (n = 4) using blue and green LEDs with different light intensities (blue LED intensities: 0.64 ~ 6.75 μW·mm<sup>-2</sup>, green LED intensities: 1.15 ~ 7.83 μW·mm<sup>-2</sup>). Light intensity of stimulus was measured at a distance of 6 cm from the screen. \* indicates a significant difference between blind mice with NW arrays and blind mice with glass implant, # indicates a significant difference between blind mice with NW arrays and normal mice (\* and #, P < 0.05, \*\*\* and ###, P < 0.001, one-way ANOVA for **d**, two-way RM ANOVA for **e** and **f**). Data are shown as mean ± SEM.

975  
976  
977  
978  
979  
980  
981  
982  
983  
984  
985  
986  
987  
988  
989  
990



991

992

993

994

995

996

997

998

999

1000

1001

1002

1003

1004

1005

1006

1007

1008

1009

1010

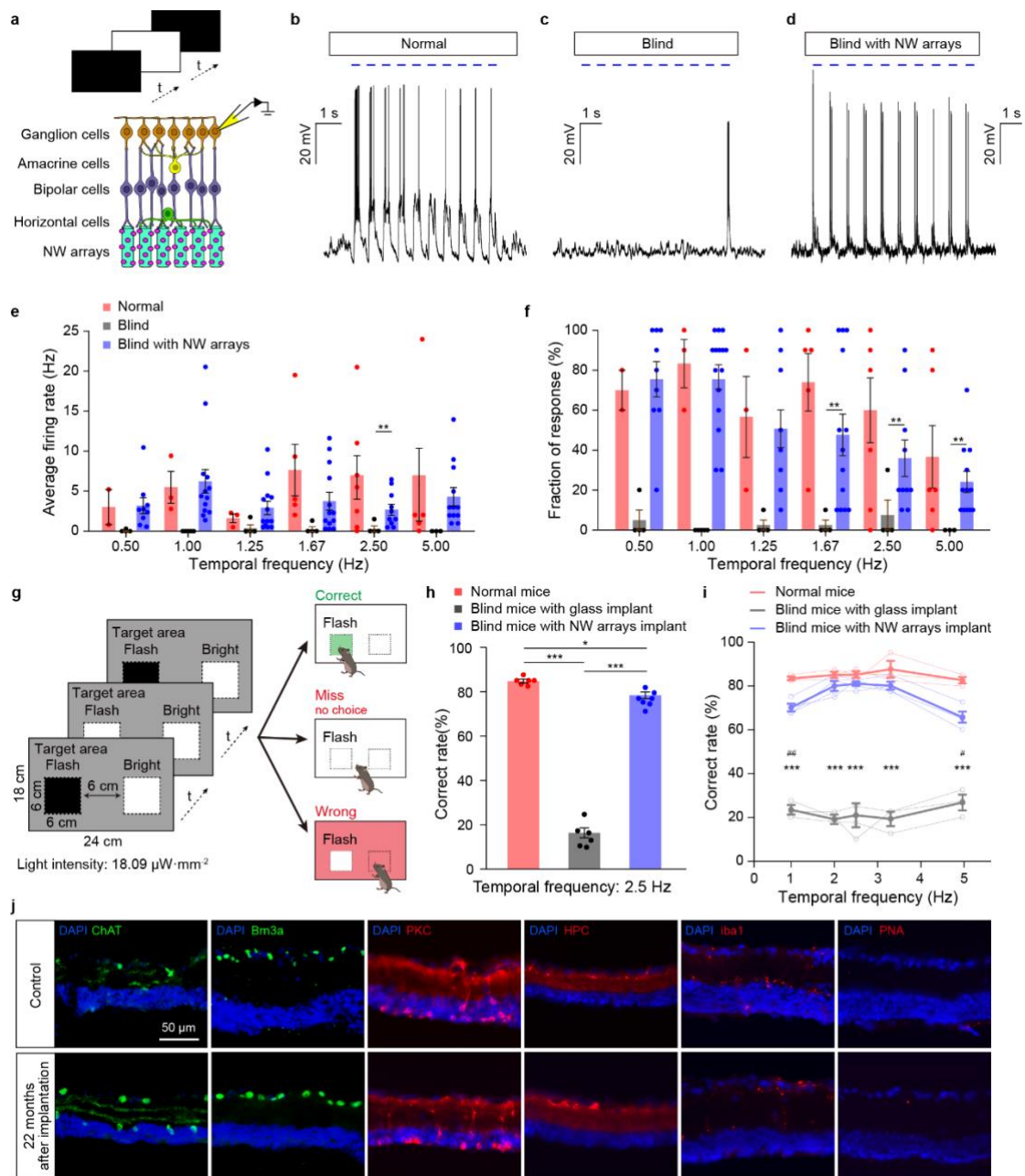
1011

1012

1013

**Fig. 2 | Responses of RGCs to moving light bars in NW arrays-attached blind retina *In vitro* and choice-box-based behavioral test using moving light bars.**

**a**, Schematics of *in vitro* patch-clamp recording of the RGCs in NW arrays-attached blind mice retina. **b-d**, RGC responded to moving light bars stimulus (wavelength: 375/28 nm, intensity: 10  $\mu\text{W}\cdot\text{mm}^{-2}$ , width: 9.6 degrees, speed: 6.85 degrees/sec) in normal, blind and NW arrays-attached blind retinas. **e-f**, Average firing rates and fraction of responses of RGCs in a normal, glass-attached and NW arrays-attached retinas using moving light bars with width ranging from 0.64 to 5.76 degrees. Normal mice: 9 RGCs from 6 retinas. Blind mice: 10 RGCs from 8 retinas. Blind mice with NW arrays attached: 16 RGCs from 10 retinas. **g**, Schematics of the choice-box-based behavioral test using moving light bar and static light bar stimulus (wavelength: 470 nm, intensity: 13.38  $\mu\text{W}\cdot\text{mm}^{-2}$ ). **h**, Correct rate of normal mice ( $n = 6$ ), blind mice with glass implant ( $n = 6$ ) and blind mice with NW arrays implant ( $n = 8$ ) in choice-box-based behavioral test using moving light bars (5.25 degrees in width at 7.85 degrees/sec). **i-j**, Correct rate of normal mice ( $n = 3$ ), blind mice with glass implant ( $n = 3$ ) and blind mice with NW arrays implant ( $n = 4$ ) in choice-box-based behavior test with moving light bars of different widths and speeds (width: 2.63 ~ 7.88 degrees, speed: 5.23 ~ 10.47 degrees/sec). All mice used in this test were over 6 months old and the blind mice in this test were implanted with NW arrays or glass for over 4 months. Light intensity of stimulus was tested at a distance of 6 cm from the screen. \* indicates a significant difference between blind mice with NW arrays and blind mice with glass implant, # indicates a significant difference between blind mice with NW arrays and normal mice (\* and #,  $P < 0.05$ , \*\* and ##,  $P < 0.01$ , \*\*\* and ###,  $P < 0.001$ , one-way ANOVA for **e**, **f** and **h**, two-way RM ANOVA for **i** and **j**). Data are shown as mean  $\pm$  SEM.



1014

1015

1016

1017

1018

1019

1020

1021

1022

1023

1024

1025

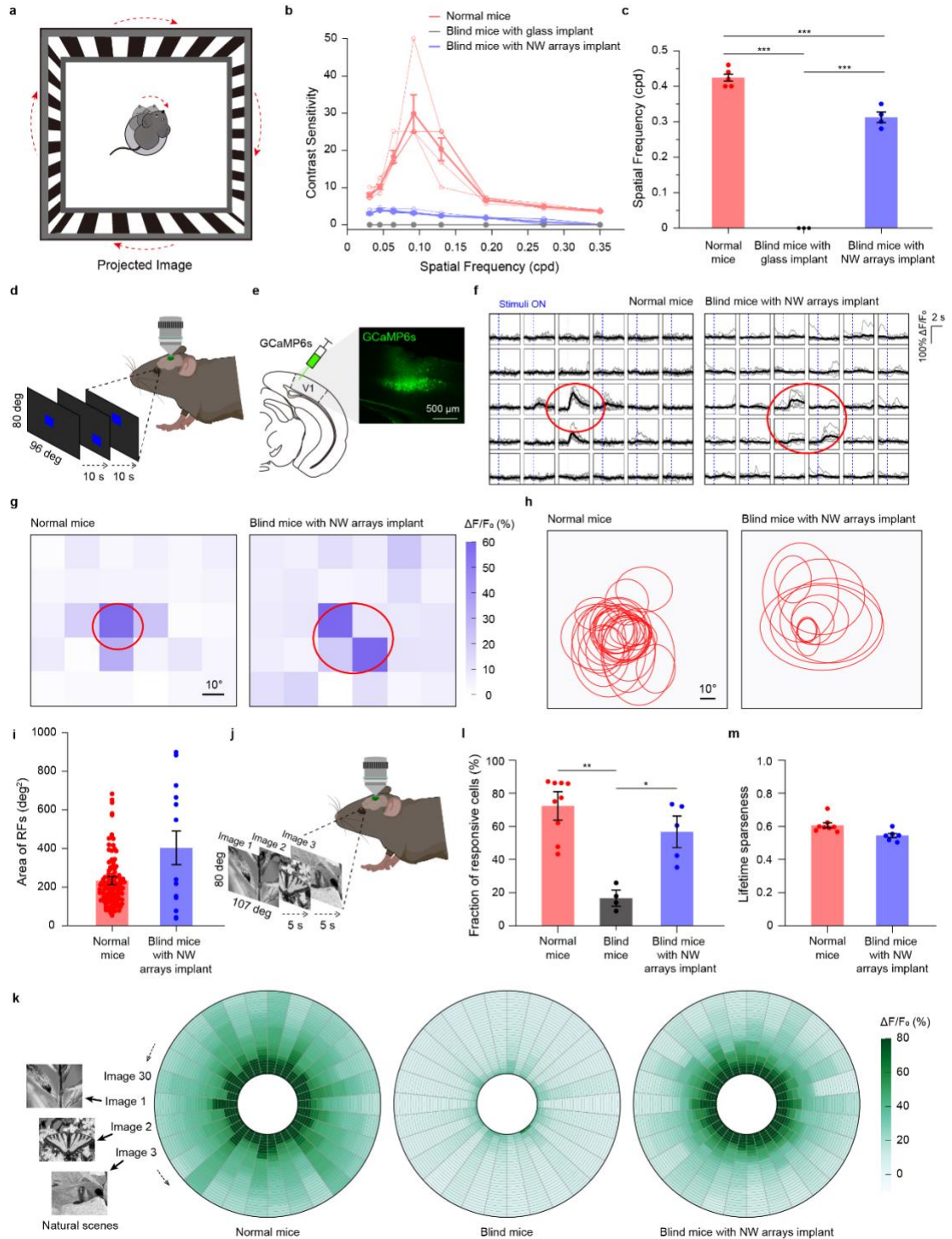
1026

1027

**Fig. 3 | *In vitro* patch clamp recording of RGCs of NW arrays-attached blind retina and choice-box-based behavioral test using flashing light.**

**a**, Schematics of *in vitro* patch clamp recording of the RGCs in NW arrays-attached blind mice retina. *t* indicates the interval of stimuli, which was equal to the duration of stimuli. **b-d**, Flashing light (wavelength: 375/28 nm, intensity: 10  $\mu\text{W}\cdot\text{mm}^{-2}$ , duration: 0.40 sec, 1.25 Hz) responses in normal, blind and NW arrays-attached blind retinas. **e-f**, Average firing rate and fraction of response of normal, glass-attached and NW arrays-attached retinas using flash visual stimulus with temporal frequency ranging from 0.50 to 5.00 Hz. Temporal frequency was calculated as 1 divided by *t*. Normal mice: 7 RGCs from 6 retinas. Blind mice: 6 RGCs from 4 retinas. Blind mice with NW arrays attached: 15 RGCs from 8 retinas. **g**, Schematics of choice-box-based behavioral test with flashing light (wavelength: 470 nm, intensity: 18.09  $\mu\text{W}\cdot\text{mm}^{-2}$ ). *t* indicates the duration of stimuli, which was equal to the interval of stimuli. **h**, Correct rate of normal mice (*n* = 6), blind mice with glass implant (*n* = 6) and blind mice with NW arrays implant (*n* = 8) in choice-box-based behavior

1028 test with flashing light stimulus at temporal frequency of 2.5 Hz ( $t = 0.2$  sec). **i**, Correct rate of  
1029 normal mice ( $n = 3$ ), blind mice with glass implant ( $n = 3$ ) and blind mice with NW arrays implant  
1030 ( $n = 4$ ) in choice-box-based behavior test with flashing light stimulus of different temporal  
1031 frequency (1.0 ~ 5.0 Hz). All mice used in this test were over 8 months old and the blind mice in  
1032 this test were implanted with NW arrays or glass for over 6 months. Light intensity of stimulus was  
1033 tested at a distance of 6 cm from the screen. **j**, Representative immunofluorescence staining of blind  
1034 mice retina with NW arrays implant for 22 months. Brn3a, RGCs. PKC- $\alpha$ , bipolar cells. HPC,  
1035 amacrine cells. iba-1, microglia. PNA, cone cells, and cone domains of the interphotoreceptor  
1036 matrix. \* indicates a significant difference between blind mice with NW arrays and blind mice with  
1037 glass implant, # indicates a significant difference between blind mice with NW arrays and normal  
1038 mice (\*\* and ##,  $P < 0.01$ , ###,  $P < 0.001$ , one-way ANOVA for **e**, **f** and **h**, two-way RM ANOVA  
1039 for **i**). Data are shown as mean  $\pm$  SEM.  
1040

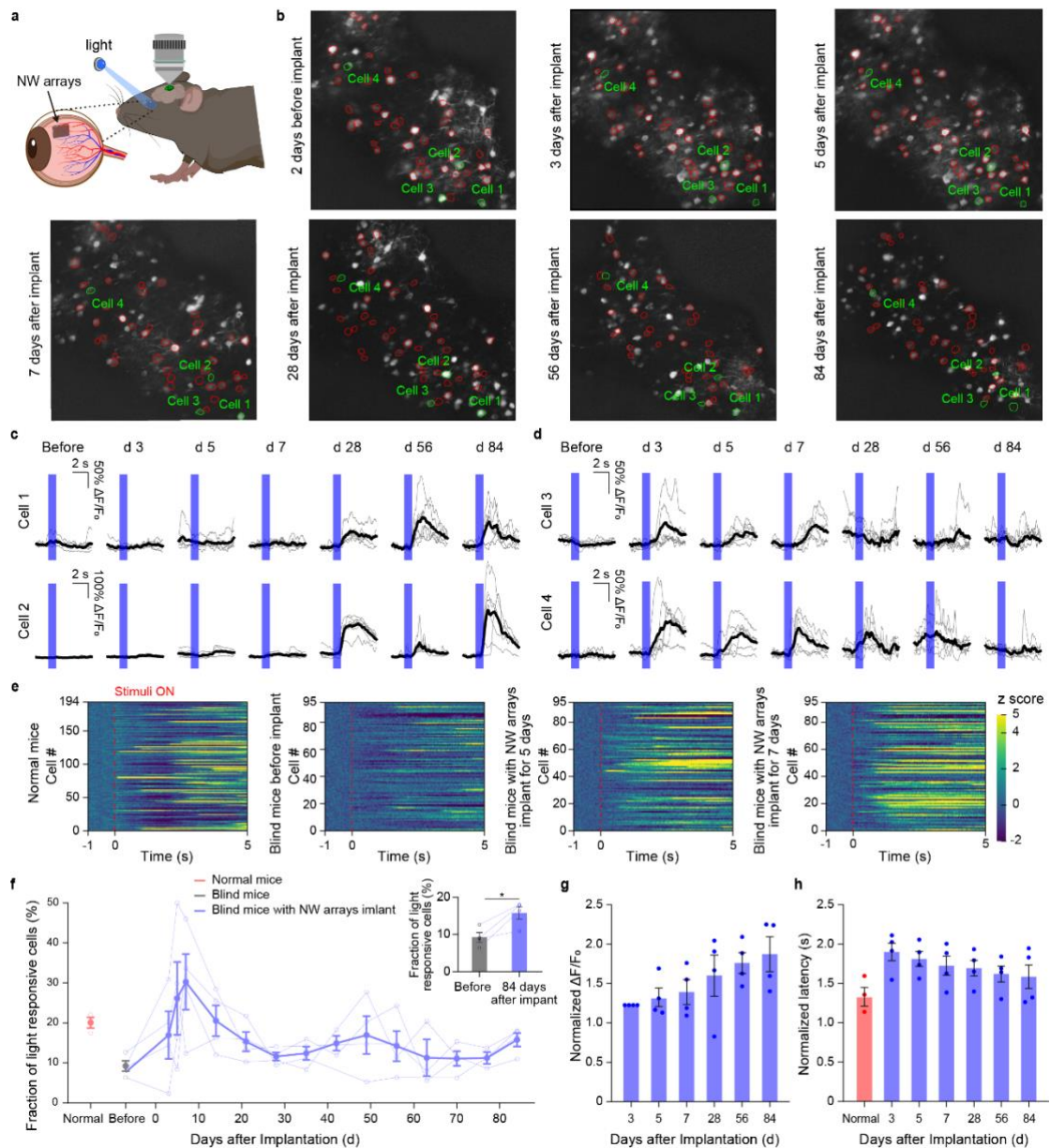


1041

1042 **Fig. 4 | Optomotor test, receptive fields and responses to natural scenes in V1 neurons of NW-**  
 1043 **implanted blind mice.**

1044 **a**, Schematics of the optomotor test. Mice were placed on a platform at the center of four screens  
 1045 displaying grating stimuli. A video camera is used to monitor the animal's behavior from above. **b**,  
 1046 Contrast sensitivity of normal mice ( $n = 5$ ), blind mice with glass implant ( $n = 3$ ), and mice with  
 1047 NW arrays implant ( $n = 4$ ) in optomotor test with different spatial frequencies of grating stimulus.  
 1048 **c**, Spatial frequency of normal mice ( $n = 5$ ), blind glass-implant mice ( $n = 3$ ), and NW-implanted  
 1049 mice ( $n = 4$ ) in optomotor test. All mice used in optomotor test were over 11 months old and the

1050 blind mice were implanted with NW arrays for more than 9 months. **d-e**, Schematics of receptive  
1051 field mapping using two-photon calcium imaging in V1. The cranial window was implanted to  
1052 medial V1, which is retinotopically corresponding to naso-dorsal retina (with NW implant). Each  
1053 blue square represented one visual stimulus consisted of  $8.75 \mu\text{W} \cdot \text{mm}^{-2}$ ,  $16 \times 16$  degree<sup>2</sup>. **f**,  
1054 GCaMP6 fluorescence signals from V1 neurons in normal mice (left) and blind mice with NW  
1055 arrays implant (right) in response to one visual stimulus (individual trace in gray, average in black)  
1056 ordered according to stimulus position. Red circles indicate the outline of calculated receptive field.  
1057 **g**, Average responses of neurons in Fig.4f. Each pixel was 16 degree by 16 degree. **h**, Distribution  
1058 of receptive fields of normal mice and blind mice with NW arrays implant. **i**, Areas of V1 receptive  
1059 field in normal mice (red,  $233.19 \text{ deg}^2$ , 111 cells from 4 mouse) and blind mice with NW arrays  
1060 implant (purple,  $402.74 \text{ deg}^2$ , 13 cells from 3 mouse). **j**, Schematics of two-photon calcium imaging  
1061 with natural scenes, which were presented for 0.5 sec followed by 5 sec inter-image gray period. **k**,  
1062 Examples of natural scenes and heatmaps of cellular responses to the natural scenes in normal mice  
1063 (left,  $n = 3$ ), blind mice (middle,  $n = 4$ ) and blind mice with NW arrays implant (right,  $n = 4$ ). Each  
1064 axial column represented responses of 30 neurons to one natural scene, with the strongest response  
1065 positioned at the core. **l**, Fraction of neurons that responded to at least one natural scene in normal  
1066 mice (72.36%,  $n = 3$ ), blind mice (16.69%,  $n = 4$ ) and blind mice with NW arrays implant (56.71%,  
1067  $n = 4$ ). **m**, Average lifetime sparseness of neurons in normal mice (0.61,  $n = 3$ ) and blind mice with  
1068 NW arrays implant (0.54,  $n = 4$ ). (\*  $P < 0.05$ , \*\*  $P < 0.01$ , \*\*\*  $P < 0.001$ , one-way ANOVA for **c**  
1069 and **l**, and student's unpaired t-test for **i** and **m**). Data are shown as mean  $\pm$  SEM.  
1070



1072

1073

1074

1075

1076

1077

1078

1079

1080

1081

1082

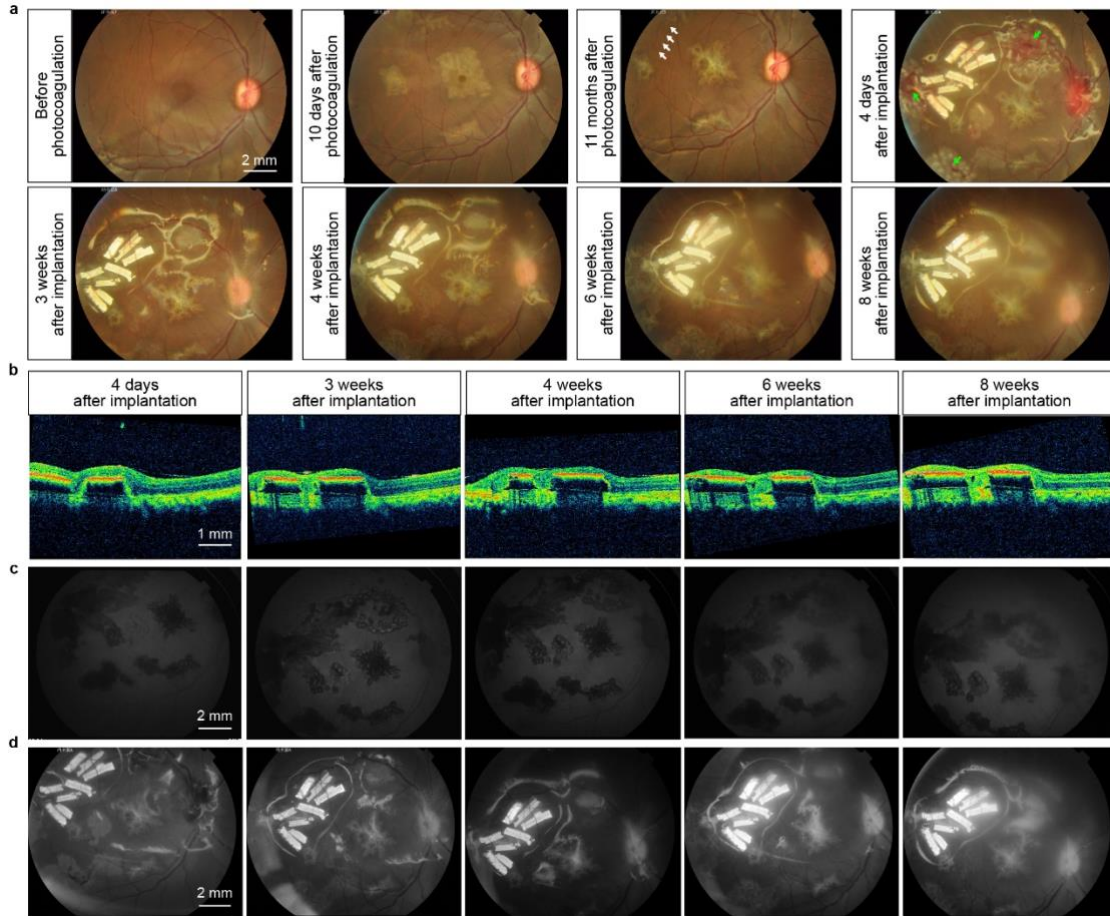
1083

1084

1085

**Fig. 5 | Long-term responses to light in V1 neurons of blind mice with NW arrays implant *in vivo*.**

**a**, Schematics of two-photon calcium imaging in V1 neurons. **b**, Four example neurons (cell 1-4, indicated with green circles) 2 days before implant surgery and 3, 5, 7, 28, 56, 84 days after NW arrays implant surgery. **c-d**, The fluorescence trace of 4 example neurons (Cell 1-4 in Fig.5b). **e**, Change of GCaMP6 fluorescence (averaged over 6 trials) in response to blue LED stimulus (wavelength: 465/25 nm, intensity:  $6.75 \mu\text{W}\cdot\text{mm}^{-2}$ , duration: 1 sec) in normal mice, blind mice before implant surgery as well as 5 and 7 days after NW implant surgery. The red dotted line indicates the onset of the blue LED stimulus. **f-h**, Fraction of light-responsive neurons, normalized  $\Delta F/F_0$  and normalized latency of normal mice (3 imaging sites from 3 mice), blind mice before and after NW arrays implant (4 imaging sites from 3 mice) (\*,  $P < 0.05$ , paired t-test for **f**). Light intensity of stimulus was tested at a distance of 6 cm from the stimulus. Data are shown as mean  $\pm$  SEM.



1086

1087

**Fig. 6 | Ophthalmological characterization of Monkey A with NW arrays implant.**

1088

**a**, Color fundus photograph of the right eye of Monkey A with eight pieces of NW arrays implanted

1089

sub-retinally. The turbid places in the fundus photograph were mainly due to the silicon oil. The

1090

white arrows indicated the perifovea area for implant surgery. The green arrows indicated

1091

photocoagulation sites to seal the opening in the retina. **b**, The retinal structure and the interface

1092

between the retina and NW arrays in OCT images of Monkey A's right eye. Red colored signals

1093

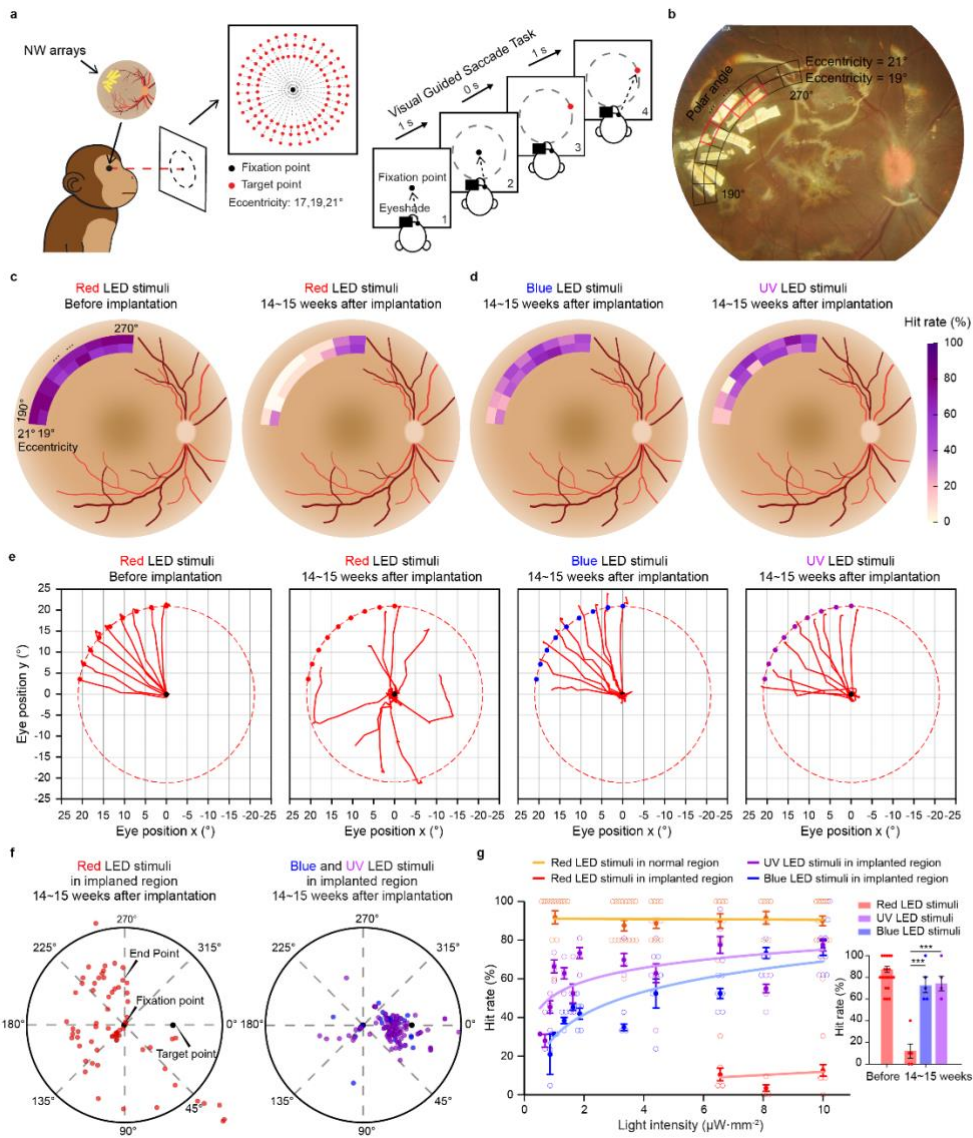
indicated the NW arrays. Dark signals indicated the glass substrate for the NW arrays. **c**, Fundus

1094

autofluorescence images of Monkey A's right eye. **d**, Red-free mode fundus photography of

1095

monkey's right eye.



1096

1097

**Fig. 7 | Visually-guided saccade behavior for Monkey A with NW arrays implant.**

1098

**a**, Schematics of visually-guided saccade (VGS) behavioral task for Monkey A with NW arrays

1099

implant (Red: 642/18 nm, Blue: 465/25 nm, UV: 360/15 nm). Monkey A is required to gaze at the

1100

fixation point centered at the screen for 1 sec, and saccade towards the target point within 1 sec. Red

1101

LEDs were placed at the fixation point. Red, blue or UV LEDs were placed at the target point.

1102

Definition of target area was illustrated in Extended Data Fig.6b. **b**, NW arrays in the fundus

1103

photograph were overlaid onto the visual field (polar angle: 190 to 270-degrees; eccentricity: 19

1104

and 21 degrees). **c**, Illustration of mean hit rates in VGS task with red LED stimuli (0.5°, polar angle:

1105

190 to 270 degrees; eccentricity: 19 and 21 degrees) before implantation (left) and 14 ~ 15 weeks

1106

after implantation (right). **d**, Illustration of mean hit rate in VGS task with blue LED (left) and UV

1107

LED stimuli (right) 14 ~ 15 weeks after implantation. **e**, The saccadic traces in response to red, blue

1108

and UV stimuli in the target point (filled red, blue and purple circles, polar angle: 190 to 270 degrees;

1109

eccentricity 21 degrees). **f**, Distribution of normalized saccadic endpoint locations (the mean eye

1110

position in a time window when the eye position was stationary 50 ~ 100 milliseconds after the peak

1111

velocity) using red (left), blue and UV (right) LED stimulus 14 ~ 15 weeks after implantation. LED

1112

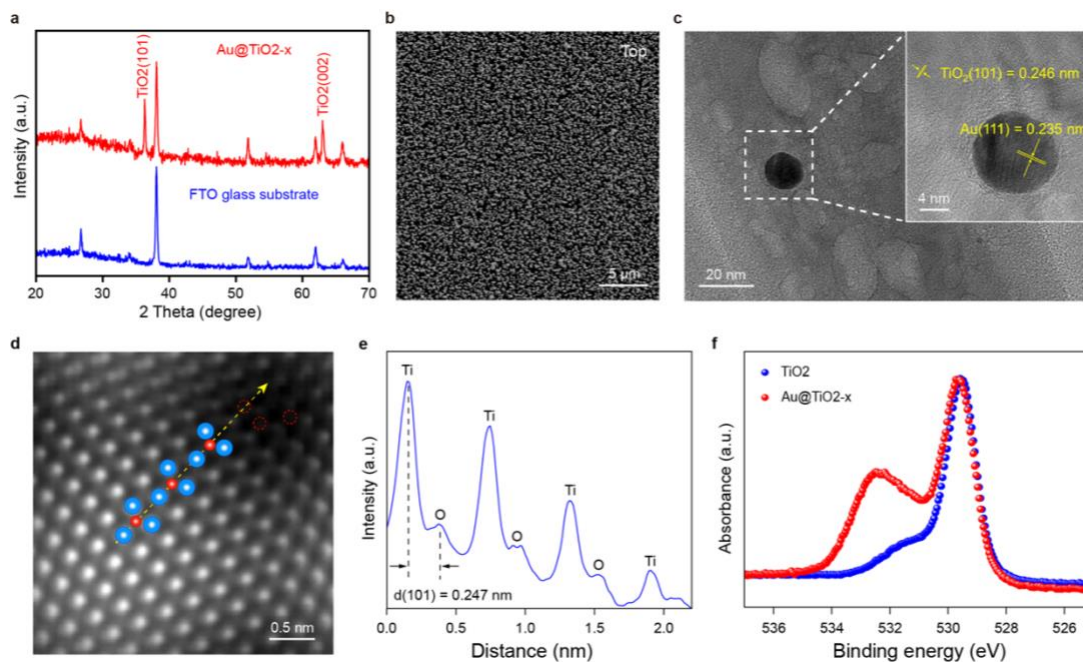
stimuli were presented at the regions defined by red rectangles in Fig.7b. **g**, Left: Hit rates of VGS

1113 task in normal regions (polar angle: 0 to 180 degrees and 280 to 350 degrees; eccentricity: 19 to 21  
1114 degrees) and NW arrays-implanted regions (eccentricity: 19 degrees or 21 degrees, polar angles:  
1115 220 to 250 degrees) for different light intensities ( $0.60 \sim 10.00 \mu\text{W}\cdot\text{mm}^{-2}$ ). Right: Mean hit rate of  
1116 VGS task using red, blue and UV LED stimulus in NW arrays-implanted regions before  
1117 implantation (red light intensity:  $7.58 \mu\text{W}\cdot\text{mm}^{-2}$ , 20 sessions) and 14 ~ 15 weeks after implantation  
1118 (light intensity:  $10.00 \mu\text{W}\cdot\text{mm}^{-2}$  for both UV and blue LED, 5 sessions). Light intensity was  
1119 measured 30 cm from the stimulus, where Monkey A conducted VGS tasks. (\*\*\*,  $P < 0.001$ , one-  
1120 way ANOVA for **g**). Red LED, 642/18 nm. Blue LED, 465/25 nm. UV LED, 360/15 nm. Data are  
1121 expressed as mean  $\pm$  SEM.

1122

1123

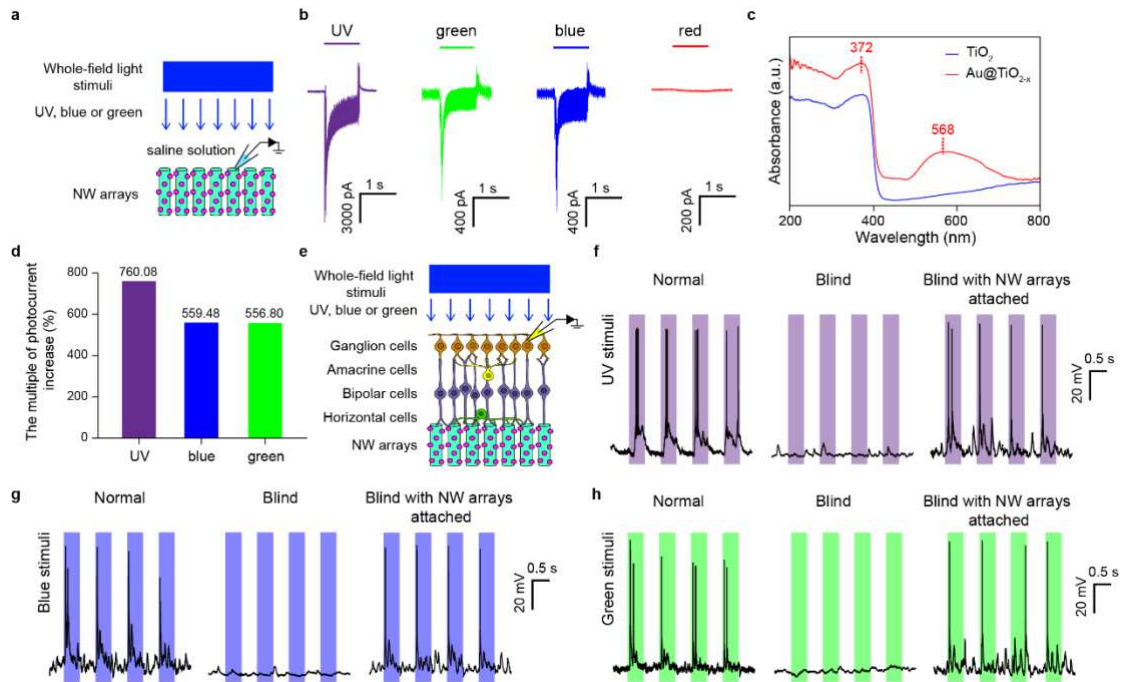
1124



1125  
 1126  
 1127  
 1128  
 1129  
 1130  
 1131  
 1132  
 1133

**Extended Data Fig. 1 | Morphology and structure characterizations of Au@TiO<sub>2-x</sub>.**

**a**, XRD pattern of FTO-coated glass substrate and Au@TiO<sub>2-x</sub> grown on FTO-coated glass substrate. **b**, Top view of Au@TiO<sub>2-x</sub>. **c**, TEM and the inserted HRTEM image of Au nanoparticles coated on TiO<sub>2</sub>-NW. **d**, Spherical aberration-corrected HAADF-STEM image of Au@TiO<sub>2-x</sub>. **e**, The corresponding intensity profiles extracted from the dashed yellow line in **b**. The blue and red balls represent the Ti and O atoms, respectively. The red dotted circles represent the oxygen vacancies. **f**, O 1s XPS spectra of original TiO<sub>2</sub> and Au@TiO<sub>2-x</sub>.

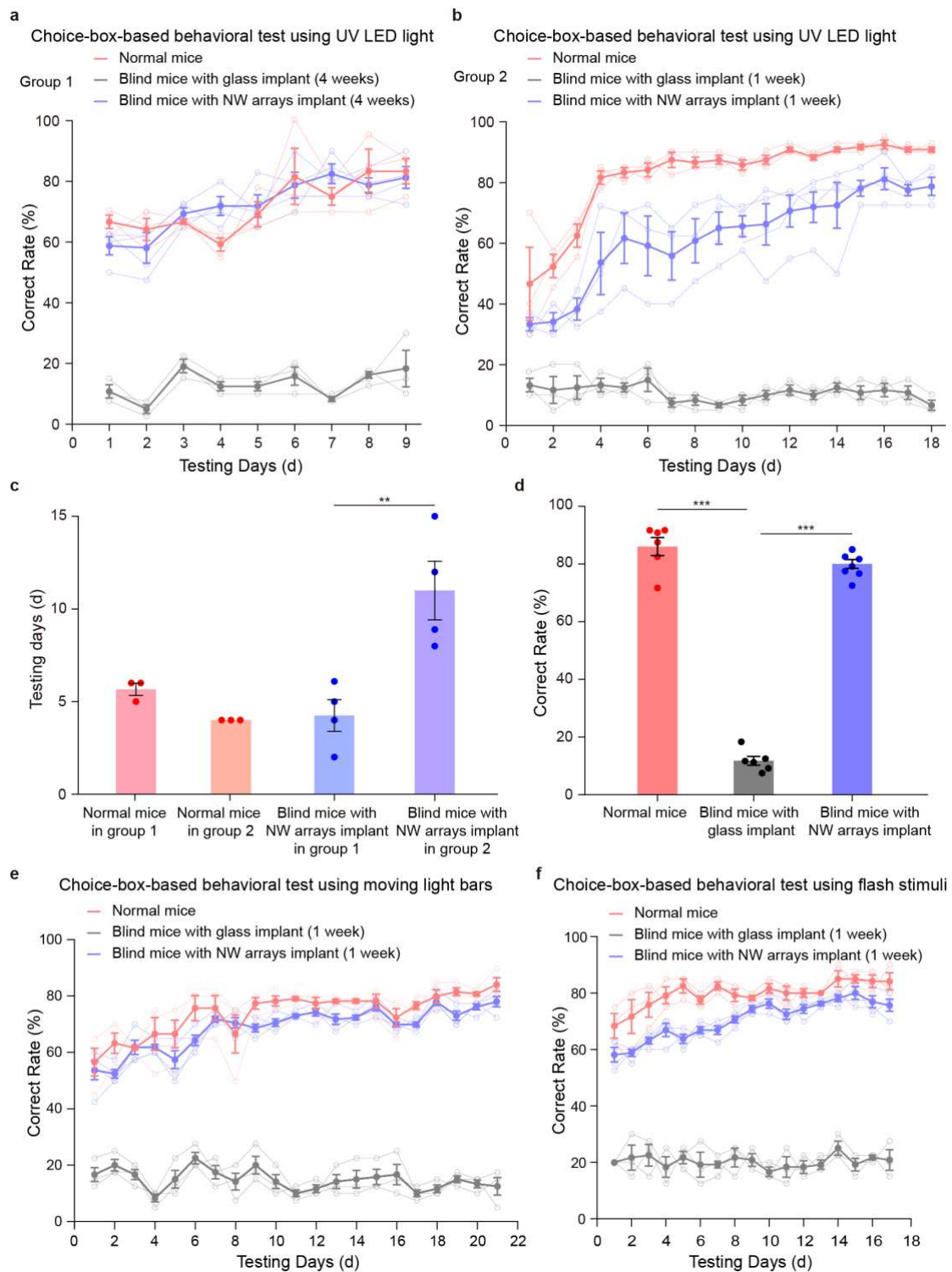


1134

1135 **Extended Data Fig. 2 | Photocurrent of  $\text{Au@TiO}_{2-x}$  NW arrays and light responses in NW**  
 1136 **arrays-attached RGCs in blind mice.**

1137 **a**, Schematic of  $\text{Au@TiO}_{2-x}$  NW arrays photocurrent measurement with UV (375/28 nm, 292.99  
 1138  $\mu\text{W}\cdot\text{mm}^{-2}$ ), blue (470/20 nm, 318.47  $\mu\text{W}\cdot\text{mm}^{-2}$ ) or green (546/12 nm, 420.38  $\mu\text{W}\cdot\text{mm}^{-2}$ ). The  
 1139 photocurrents were measured by Ag/AgCl electrodes attached to the surface of the NW arrays in  
 1140 normal saline solution. **b**, Photocurrents generated by illumination of UV, blue, green and red light,  
 1141 receptively by an  $\text{Au@TiO}_{2-x}$  NW arrays. **c**, UV-visible absorbance spectra of original  $\text{TiO}_2$  and  
 1142  $\text{Au@TiO}_{2-x}$ . **d**, Compared with the published results<sup>26</sup>, the photocurrent of improved NW arrays  
 1143 increased by 760.08%, 559.48% and 556.80% under UV, blue and green light, receptively. **e**,  
 1144 Schematic of light responses recoding of NW arrays-attached RGCs in blind mice. **f-h**, Responses  
 1145 of RGCs in wild-type, blind and NW arrays-attached blind retinas with UV, blue and green light  
 1146 stimulation, respectively. Horizontal color bars represent the light stimulation color and duration  
 1147 (UV, 375/28 nm, 292.99  $\mu\text{W}\cdot\text{mm}^{-2}$ . Blue, 470/20 nm, 318.47  $\mu\text{W}\cdot\text{mm}^{-2}$ . Green, 546/12 nm, 420.38  
 1148  $\mu\text{W}\cdot\text{mm}^{-2}$ . Duration, 0.5 sec).

1149



1150

1151

**Extended Data Fig. 3 | Choice-box-based behavioral test using LED light, moving bars and flash stimuli at different days of NW-array implant.**

1152

1153

**a**, Correct rates of normal mice ( $n = 3$ ), blind mice with glass implant ( $n = 3$ ) and blind mice with

1154

NW arrays-implanted for 4 weeks ( $n = 4$ ) in the choice-box-based behavior test using a UV LED

1155

( $375/15 \text{ nm}$ ,  $6.24 \mu\text{W}\cdot\text{mm}^{-2}$ ). **b**, Correct rates of normal mice ( $n = 3$ ), blind mice with glass implant

1156

( $n = 3$ ) and blind mice with NW arrays-implanted for 1 week ( $n = 4$ ) in the choice-box-based

1157

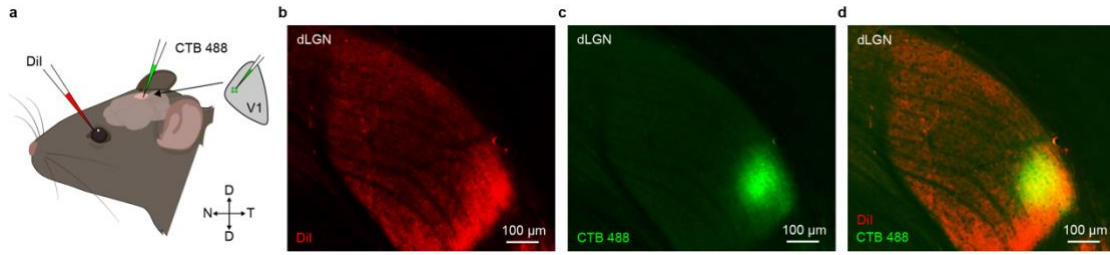
behavior test using a UV LED ( $375/15 \text{ nm}$ ,  $6.24 \mu\text{W}\cdot\text{mm}^{-2}$ ). **c**, Number of testing days when the

1158

correct rate reached 70% and maintained steady for 3 days in normal mice in two different groups

1159 (normal mice group 1 and group 2) and blind mice with NW arrays-implanted for 4 weeks or 1 week  
1160 after implantation in the choice-box-based behavioral test. **d**, Correct rates of normal mice (n = 6),  
1161 blind mice with glass implant (n = 6) and blind mice with NW arrays implant (n = 8) at the same  
1162 time in **c**. **e**, Correct rates of normal mice (n = 3), blind mice with glass implant (n = 3) and blind  
1163 mice with NW arrays-implanted for 1 week (n = 4) in the choice-box-based behavior test using  
1164 moving light bars (5.25 degrees, 7.85 degrees/sec, 13.38  $\mu\text{W}\cdot\text{mm}^{-2}$ ). **f**, Correct rates of normal mice  
1165 (n = 3), blind mice with glass implant (n = 3) and blind mice with NW arrays-implanted for 1 week  
1166 (n = 4) in the choice-box-based behavior test using flashing light. \* indicates a significant difference  
1167 (\*\*,  $P < 0.01$ . \*\*\*,  $P < 0.001$ , one-way ANOVA for **c** and **d**). Data are expressed as mean  $\pm$  SEM.  
1168

1169

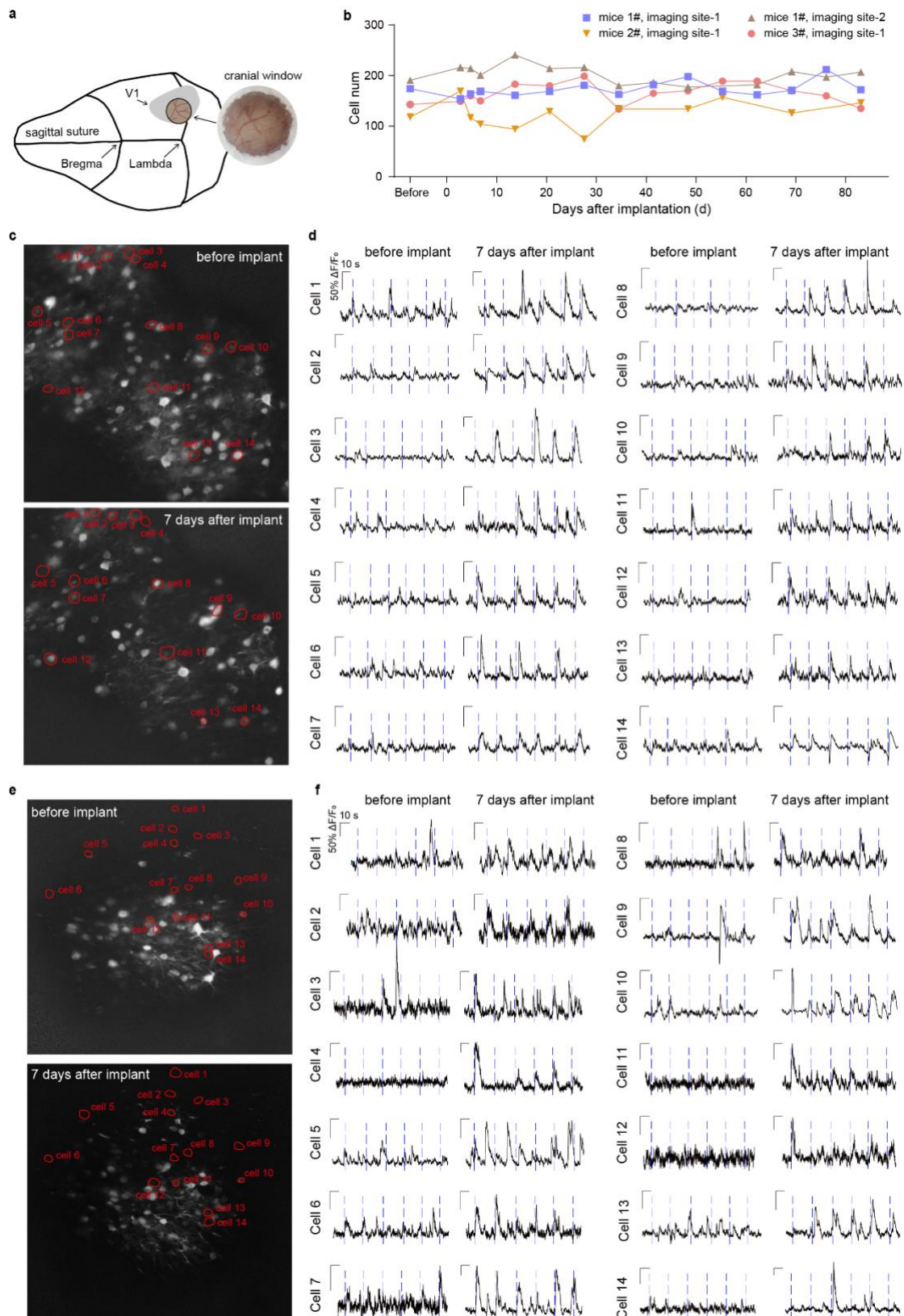


1170

1171 **Extended Data Fig. 4 | Position of NW-implant in the retina and its corresponding retinotopic**  
1172 **position in the visual cortex in mice.**

1173 **a**, Fluorescence dye (DiI) were injected introvitreally into mouse's dorsal retina (where NW was  
1174 implanted). CTB-488 was injected into lateral V1. **b-d**, DiI (from the retina) and CTB-488 (from  
1175 V1) signals in the dLGN.

1176

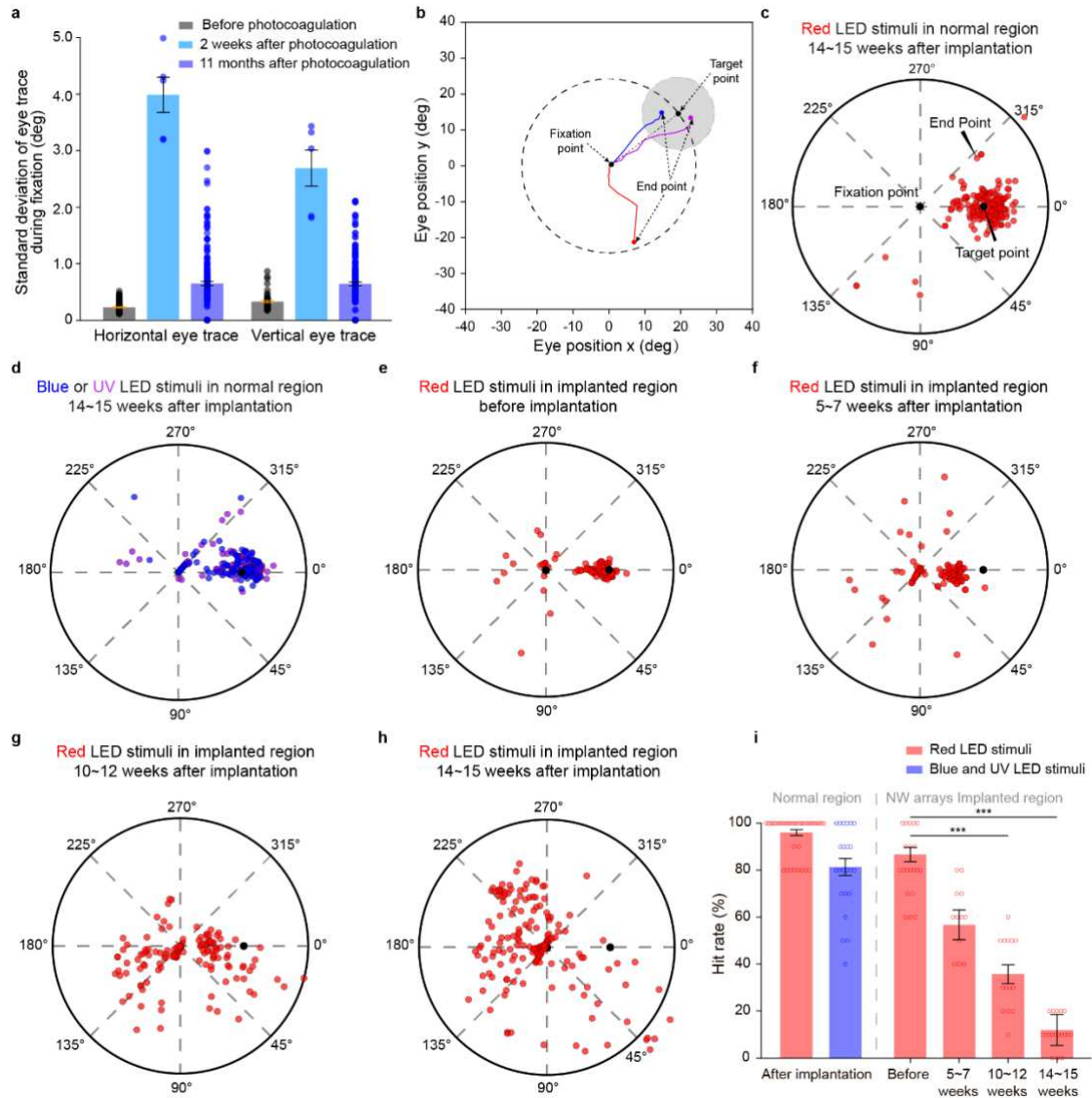


1177

1178 **Extended Data Fig. 5 | Long-term light-evoked responses using two-photon calcium imaging**  
 1179 **in V1 of NW-implanted blind mice *in vivo*.**

1180 **a**, Schematic of the position of the cranial window in V1 and close-up of the completed cranial  
 1181 window on the day of surgery. **b**, Number of neurons recorded at different time points throughout

1182 the experiment. **c and e**, Grayscale image of recording field of two blind mice before implant and 7  
1183 days after implant. 14 representative light-responsive neurons were marked by red contour. **d and**  
1184 **f**, The fluorescence change of neurons in Extended Data Fig.5 c, e in response to visual stimulation  
1185 (Blue LED, 465/25 nm,  $6.75 \mu\text{W}\cdot\text{mm}^{-2}$ , duration: 1 second). Blue dotted lines indicate the onset  
1186 time of the visual stimulation.



1187

1188 **Extended Data Fig. 6 | VGS performance in Monkey A.**

1189 **a**, Standard deviation of Monkey A's horizontal and vertical eye trace during fixation before  
 1190 photocoagulation, 2 weeks and 11 months after photocoagulation. **b**, Schematic of VGS task. The  
 1191 gray area indicates a 15-degree circular region surrounding the target point (defined as target area,  
 1192 gray region in the figure). **c-d**, Distribution of normalized saccadic endpoints in normal retinal  
 1193 regions (eccentricities: 19 and 21 degrees, polar angles: 40, 50 and 130 degrees) with red (642/18  
 1194 nm), blue (465/25 nm) or UV (360/15 nm) LED stimuli. **e-h**, Distribution of normalized saccadic  
 1195 endpoints using red LED in NW-arrays implanted region (eccentricities: 19 and 21 degrees, polar  
 1196 angles: 200 ~ 250 degrees) before implantation, 5 ~ 7 weeks after implantation, 10 ~ 12 weeks  
 1197 after implantation, and 14 ~ 15 weeks after implantation. **i**, Mean hit rates of VGS task in Extended Data  
 1198 Fig.7 c-h. \* indicates significant difference (\*\*\*,  $P < 0.001$ , one-way ANOVA for **i**). Red LED,  
 1199 642/18 nm. UV LED, 360/15 nm. Blue LED, 465/25 nm. Data are expressed as mean  $\pm$  SEM.

1200 **Extended Data Table 1** | Summary of in-vitro photocurrent with the corresponding duration and  
 1201 in-vivo response with the corresponding duration using semiconductors as artificial photoreceptors.

Semiconductors	Light source	In-vitro photocurrent (pA)	In-vitro duration (second)	In-vivo response (mV)	In-vivo duration (second)	References
Au@TiO <sub>2-x</sub>	UV (375 nm, 292.99 μW·mm <sup>-2</sup> )	~ 13100	~ 1	~ 40	~ 0.1	This work
	Blue (470 nm, 318.47 μW·mm <sup>-2</sup> )	~ 1300	~ 1	~ 50	~ 0.1	
	Green (546 nm, 420.38 μW·mm <sup>-2</sup> )	~ 1100	~ 1	~ 50	~ 0.1	
Au@TiO <sub>2</sub>	UV (375 nm, 133 μW·mm <sup>-2</sup> )	~ 1400	~ 1	~ 40	~ 0.05	Nat. Commun. 2018, 9, 786 <sup>26</sup>
	Blue (470 nm, 691 μW·mm <sup>-2</sup> )	~ 100	~ 1	~ 80	~ 0.05	
	Green (546 nm, 470 μW·mm <sup>-2</sup> )	~ 100	~ 1	~ 60	~ 0.05	
Poly(3-hexylthiophene)	Green (532 nm, 15000 μW·mm <sup>-2</sup> )	~ 250	~ 0.02	/	/	Nat. Photonics 2013, 7, 400 <sup>68</sup>
	Green (532 nm, 4000 μW·mm <sup>-2</sup> )	/	/	~ 0.1	~ 0.01	
PEDOT:PSS	Green (530 nm, 2*10 <sup>5</sup> μW·mm <sup>-2</sup> )	/	/	~ 0.167	~ 0.0004	Nat. Mater. 2017, 7, 400 <sup>69</sup>
Formamidineum lead iodide	Green (500 nm, 2000 μW·mm <sup>-2</sup> )	~ 2*10 <sup>6</sup>	~ 0.3	/	/	Nature 2020, 581, 278 <sup>22</sup>
Au@Si*	Green (530 nm, ~ 4000 μW·mm <sup>-2</sup> )	~ 10000	~ 0.01	/	/	Nat Biomed Eng. 2018, 2, 508 <sup>29,70</sup>
	Green (530 nm, ~ 7000 μW·mm <sup>-2</sup> )	~ 16000	~ 0.01	/	/	
	Green (530 nm, 60000 μW·mm <sup>-2</sup> )	85775	~ 0.01	/	/	
	Green (532 nm, 1.9*10 <sup>9</sup> μW·mm <sup>-2</sup> )	/	/	~ 50	~ 0.012	
	Blue (473 nm, 85000 μW·mm <sup>-2</sup> )	/	/	~ 0.04	~ 0.0005	

1202 Notes: \* represent the Au@Si semiconductor was used in the bio-interface with brain slice.

1203

Positions of saccadic target point		Hit Rate (%)			
		Before implantation:	14 ~ 15 weeks after implantation:		
Eccentricity (degree)	Polar angle (degree)	Red LED	Red LED	Blue LED	UV LED
19	190	86	40	40	20
	200	100	0	26	40
	210	93	10	50	50
	220	66	10	46	60
	230	80	10	60	20
	240	100	10	80	70
	250	73	30	85	70
	260	80	50	55	40
	270	73	70	50	60
21	190	100	10	20	20
	200	100	0	30	30
	210	93	0	40	0
	220	80	0	60	70
	230	86	0	40	80
	240	86	10	70	60
	250	93	10	50	50
	260	100	40	40	90
	270	100	60	60	70

1206

**Extended Data Table 3** | Statistical detail information for figures

1207

Fig. 1d UV	Normal mice (Normal) VS Blind mice with Glass implant (Glass)	Normal: n=3, Glass: n=3	One-way ANOVA with Tukey post-hoc test.	F=1.977, P<0.001
Fig. 1d UV	Normal VS Blind mice with NW arrays implant (NW arrays)	Normal: n=3, NW arrays: n=4	One-way ANOVA with Tukey post-hoc test.	F=1.977, P=0.0236
Fig. 1d UV	Glass VS NW arrays	Glass: n=3, NW arrays: n=4	One-way ANOVA with Tukey post-hoc test.	F=1.977, P<0.001
Fig. 1d Green	Normal VS Glass	Normal: n=3, Glass: n=3	One-way ANOVA with Tukey post-hoc test.	F=1.141, P<0.001
Fig. 1d Green	Glass VS NW arrays	Glass: n=3, NW arrays: n=4	One-way ANOVA with Tukey post-hoc test.	F=1.141, P<0.001
Fig. 1d Blue	Normal VS Glass	Normal: n=3, Glass: n=3	One-way ANOVA with Tukey post-hoc test.	F=1.235, P<0.001
Fig. 1d Blue	Glass VS NW arrays	Glass: n=3, NW arrays: n=4	One-way ANOVA with Tukey post-hoc test.	F=1.235, P<0.001
Fig. 1e 0.64 $\mu\text{W}\cdot\text{mm}^{-2}$	Normal VS NW arrays	Normal: n=3, NW arrays: n=4	One-way ANOVA with Tukey post-hoc test.	F=0.3425, P<0.001
Fig. 1e 0.64 $\mu\text{W}\cdot\text{mm}^{-2}$	Glass VS NW arrays	Glass: n=3, NW arrays: n=4	One-way ANOVA with Tukey post-hoc test.	F=0.3425, P<0.001
Fig. 1e 1.53 $\mu\text{W}\cdot\text{mm}^{-2}$	Normal VS NW arrays	Normal: n=3, NW arrays: n=4	One-way ANOVA with Tukey post-hoc test.	F=0.3164, P<0.001
Fig. 1e 1.53 $\mu\text{W}\cdot\text{mm}^{-2}$	Glass VS NW arrays	Glass: n=3, NW arrays: n=4	One-way ANOVA with Tukey post-hoc test.	F=0.3164, P<0.001
Fig. 1e 2.93 $\mu\text{W}\cdot\text{mm}^{-2}$	Glass VS NW arrays	Glass: n=3, NW arrays: n=4	One-way ANOVA with Tukey post-hoc test.	F=0.4800, P<0.001

Fig. 1e 3.31 $\mu\text{W}\cdot\text{mm}^{-2}$	Glass VS NW arrays	Glass: n=3, NW arrays: n=4	One-way ANOVA with Tukey post-hoc test.	F=0.5706, P<0.001
Fig. 1e 6.75 $\mu\text{W}\cdot\text{mm}^{-2}$	Glass VS NW arrays	Glass: n=3, NW arrays: n=4	One-way ANOVA with Tukey post-hoc test.	F=1.236, P<0.001
Fig. 1f 1.15 $\mu\text{W}\cdot\text{mm}^{-2}$	Normal VS NW arrays	Normal: n=3, NW arrays: n=4	One-way ANOVA with Tukey post-hoc test.	F=0.1522, P<0.001
Fig. 1f 1.15 $\mu\text{W}\cdot\text{mm}^{-2}$	Glass VS NW arrays	Glass: n=3, NW arrays: n=4	One-way ANOVA with Tukey post-hoc test.	F=0.1522, P<0.001
Fig. 1f 2.04 $\mu\text{W}\cdot\text{mm}^{-2}$	Normal VS NW arrays	Normal: n=3, NW arrays: n=4	One-way ANOVA with Tukey post-hoc test.	F=0.1026, P<0.001
Fig. 1f 2.04 $\mu\text{W}\cdot\text{mm}^{-2}$	Glass VS NW arrays	Glass: n=3, NW arrays: n=4	One-way ANOVA with Tukey post-hoc test.	F=0.1026, P<0.001
Fig. 1f 4.20 $\mu\text{W}\cdot\text{mm}^{-2}$	Normal VS NW arrays	Normal: n=3, NW arrays: n=4	One-way ANOVA with Tukey post-hoc test.	F=1.141, P<0.001
Fig. 1f 4.20 $\mu\text{W}\cdot\text{mm}^{-2}$	Glass VS NW arrays	Glass: n=3, NW arrays: n=4	One-way ANOVA with Tukey post-hoc test.	F=1.141, P<0.001
Fig. 1f 7.83 $\mu\text{W}\cdot\text{mm}^{-2}$	Normal VS NW arrays	Normal: n=3, NW arrays: n=4	One-way ANOVA with Tukey post-hoc test.	F=0.3786, P=0.004
Fig. 1f 7.83 $\mu\text{W}\cdot\text{mm}^{-2}$	Glass VS NW arrays	Glass: n=3, NW arrays: n=4	One-way ANOVA with Tukey post-hoc test.	F=0.3786, P<0.001
Fig. 2e 1.92 degree	Normal VS Blind	Normal: n=9, Blind: n=10	One-way ANOVA with Tukey post-hoc test.	F=3.013, P=0.0419
Fig. 2e 5.76 degree	Blind VS NW arrays	Blind: n=10, NW arrays: n=16	One-way ANOVA with Tukey post-hoc test.	F=2.110, P=0.0043
Fig. 2f 3.20 degree	Blind VS NW arrays	Blind: n=10, NW arrays: n=16	One-way ANOVA with Tukey post-hoc test.	F=6.679, P=0.0161

Fig. 2f 3.84 degree	Blind VS NW arrays	Blind: n=10, NW arrays: n=16	One-way ANOVA with Tukey post-hoc test.	F=6.640, P=0.0077
Fig. 2f 5.12 degree	Normal VS Blind	Normal: n=9, Blind: n=10	One-way ANOVA with Tukey post-hoc test.	F=2.035, P=0.0182
Fig. 2f 5.76 degree	Normal VS Blind	Normal: n=9, Blind: n=10	One-way ANOVA with Tukey post-hoc test.	F=1.975, P=0.0199
Fig. 2h 2.63 degree	Normal VS NW arrays	Normal: n=3, NW arrays: n=4	Two-way RM ANOVA test with Tukey post-hoc test.	F=0.3912, P=0.0179
Fig. 2h 2.63 degree	Glass VS NW arrays	Glass: n=3, NW arrays: n=4	Two-way RM ANOVA test with Tukey post-hoc test.	F=0.3912, P<0.001
Fig. 2h 3.94 degree	Glass VS NW arrays	Glass: n=3, NW arrays: n=4	Two-way RM ANOVA test with Tukey post-hoc test.	F=0.7000, P<0.001
Fig. 2h 5.25 degree	Glass VS NW arrays	Glass: n=3, NW arrays: n=4	Two-way RM ANOVA test with Tukey post-hoc test.	F=0.06891, P<0.001
Fig. 2h 6.57 degree	Glass VS NW arrays	Glass: n=3, NW arrays: n=4	Two-way RM ANOVA test with Tukey post-hoc test.	F=0.6192, P<0.001
Fig. 2h 7.88 degree	Glass VS NW arrays	Glass: n=3, NW arrays: n=4	Two-way RM ANOVA test with Tukey post-hoc test.	F=0.8694, P<0.001
Fig. 2i 5.23 degree/s	Glass VS NW arrays	Glass: n=3, NW arrays: n=4	Two-way RM ANOVA test with Tukey post-hoc test.	F=0.2753, P<0.001
Fig. 2i 6.54 degree/s	Glass VS NW arrays	Glass: n=3, NW arrays: n=4	Two-way RM ANOVA test with Tukey post-hoc test.	F=0.3595, P<0.001
Fig. 2i 7.85 degree/s	Glass VS NW arrays	Glass: n=3, NW arrays: n=4	Two-way RM ANOVA test with Tukey post-hoc test.	F=0.6891, P<0.001
Fig. 2i 9.18 degree/s	Glass VS NW arrays	Glass: n=3, NW arrays: n=4	Two-way RM ANOVA test with Tukey post-hoc test.	F=0.5623, P<0.001

Fig. 2i 10.47 degree/s	Glass VS NW arrays	Glass: n=3, NW arrays: n=4	Two-way RM ANOVA test with Tukey post-hoc test.	F=0.1000, P<0.001
Fig. 3e 2.5 Hz	Blind VS NW arrays	Blind: n=6, NW arrays: n=15	One-way ANOVA with Tukey post-hoc test.	F=3.864, P=0.0086
Fig. 3f 1.67 Hz	Blind VS NW arrays	Blind: n=6, NW arrays: n=15	One-way ANOVA with Tukey post-hoc test.	F=2.720, P=0.00824
Fig. 3f 2.50 Hz	Blind VS NW arrays	Blind: n=6, NW arrays: n=15	One-way ANOVA with Tukey post-hoc test.	F=1.422, P=0.00482
Fig. 3f 5.00 Hz	Blind VS NW arrays	Blind: n=6, NW arrays: n=15	One-way ANOVA with Tukey post-hoc test.	F=2.085, P=0.00308
Fig. 3h 1 Hz	Normal VS NW arrays	Normal: n=3, NW arrays: n=4	Two-way RM ANOVA test with Tukey post-hoc test.	F=0.5765, P=0.0023
Fig. 3h 1 Hz	Glass VS NW arrays	Glass: n=3, NW arrays: n=4	Two-way RM ANOVA test with Tukey post-hoc test.	F=0.5765, P<0.001
Fig. 3h 2 Hz	Glass VS NW arrays	Glass: n=3, NW arrays: n=4	Two-way RM ANOVA test with Tukey post-hoc test.	F=0.09172, P<0.001
Fig. 3h 2.5 Hz	Glass VS NW arrays	Glass: n=3, NW arrays: n=4	Two-way RM ANOVA test with Tukey post-hoc test.	F=1.644, P<0.001
Fig. 3h 3.3 Hz	Glass VS NW arrays	Glass: n=3, NW arrays: n=4	Two-way RM ANOVA test with Tukey post-hoc test.	F=0.1201, P<0.001
Fig. 3h 5 Hz	Normal VS NW arrays	Normal: n=3, NW arrays: n=4	Two-way RM ANOVA test with Tukey post-hoc test.	F=0.4393, P=0.0071
Fig. 3h 5 Hz	Glass VS NW arrays	Glass: n=3, NW arrays: n=4	Two-way RM ANOVA test with Tukey post-hoc test.	F=0.4393, P<0.001
Fig. 4c	Normal VS Glass	Normal: n=5, Glass: n=3	One-way ANOVA with Tukey post-hoc test.	F=3.102, P<0.001

Fig. 4c	Normal VS NW arrays	Normal: n=5, NW arrays: n=4	One-way ANOVA with Tukey post-hoc test.	F=3.102, P=0.002
Fig. 4c	Glass VS NW arrays	Glass: n=3, NW arrays: n=4	One-way ANOVA with Tukey post-hoc test.	F=3.102, P<0.001
Fig. 4i	Normal VS NW arrays	Normal: n=111, NW arrays: n=13	Unpaired t-test	t=4.098, P=0.072
Fig. 4l	Normal VS Blind	Normal: n=3, Blind: n=4	One-way ANOVA with Tukey post-hoc test.	F=1.010, P=0.0047
Fig. 4l	Blind VS NW arrays	Blind: n=4, NW arrays: n=4	One-way ANOVA with Tukey post-hoc test.	F=1.010, P=0.0207
Fig. 4m	Normal VS NW arrays	Normal: n=8, NW arrays: n=6	Unpaired t-test	t=1.632, P=0.1287
Fig. 5d	Before VS 84 days after implant	Before: n=3, 84 days after implant: n=3	Paired t-test	t=3.112, P=0.0358
Fig. 7f	14~15 weeks: Red VS Blue	Red: n=5, Blue: 4	One-way ANOVA with Tukey post-hoc test.	F=0.06668, P=0.006
Fig. 7f	14~15 weeks: Red VS UV	Red: n=5, UV: n=5	One-way ANOVA with Tukey post-hoc test.	F=0.06668, P=0.003
Extended Data Fig. 3c	Blind mice with NW arrays implant in group 1 VS group 2	Group 1: n=4, Group 2: n=4	One-way ANOVA with Tukey post-hoc test.	F=4.707, p=0.0094
Extended Data Fig. 3d	Normal VS NW arrays	Normal: n=6, NW arrays: n=6	One-way ANOVA with Tukey post-hoc test.	F=8.001, P<0.001
Extended Data Fig. 3d	Glass VS NW arrays	Glass: n=6, NW arrays: n=6	One-way ANOVA with Tukey post-hoc test.	F=8.001, P<0.001
Extended Data Fig. 6i	Before VS 10~12 weeks	Before: n=20, 10~12 weeks: n=14	One-way RM ANOVA with Dunnett post-hoc test	F=3.197, P<0.001
Extended Data Fig. 6i	Before VS 14~15 weeks	Before: n=20, 14~15 weeks: n=18	One-way RM ANOVA with Dunnett post-hoc test	F=3.197, P<0.001

1209 **Extended Data Movie 1** | Choice-box-based behavioral test of normal mice, blind mice with glass  
1210 implant and blind mice with NW arrays implant using green LED stimulus.  
1211  
1212 **Extended Data Movie 2** | Choice-box-based behavioral test of normal mice, blind mice with glass  
1213 implant and blind mice with NW arrays implant using moving visual stimulus.  
1214  
1215 **Extended Data Movie 3** | Choice-box-based behavioral test of normal mice, blind mice with glass  
1216 implant and blind mice with NW arrays implant using flash visual stimulus.  
1217  
1218 **Extended Data Movie 4** | Visual acuity and contrast sensitivity test of normal mice, blind mice with  
1219 glass implant and blind mice with NW arrays implant.  
1220  
1221 **Extended Data Movie 5** | Light-evoked responses in V1 neurons through two-photon calcium  
1222 imaging recording of normal mice, blind mice before implantation and 7 days after implantation.  
1223  
1224 **Extended Data Movie 6** | Visually-guided saccade task of monkey A with red LED stimulus in  
1225 region of implantation and control.  
1226  
1227 **Extended Data Movie 7** | Visually-guided saccade task of monkey A with blue LED stimulus in  
1228 region of implantation and control.  
1229  
1230

## Supplementary Files

This is a list of supplementary files associated with this preprint. Click to download.

- [ExtendedDataMovie1.ChoiceboxbasedbehavioraltestwithgreenLEDlightstimulus.mp4](#)
- [ExtendedDataMovie2.Choiceboxbasedbehavioraltestwithmovingvisualstimulus.mp4](#)
- [ExtendedDataMovie3.Choiceboxbasedbehavioraltestwithflashvisualstimulus.mp4](#)
- [ExtendedDataMovie4.Visualacuityandcontrastssensitivitytest.mp4](#)
- [ExtendedDataMovie5.LightevokedresponsesinV1neuronsthroughtwophotoncalciumimagingrecording.mp4](#)
- [ExtendedDataMovie6.VisualguidedssaccadetaskwithRedLedstimulus.mp4](#)
- [ExtendedDataMovie7.VisualguidedssaccadetaskwithBlueLedstimulus.mp4](#)